


Research Article

# Therapeutic potential of metal ions for COVID-19: insights from the papain-like protease of SARS-CoV-2

Cameron Lee Shetler<sup>1</sup>, Juliana C. Ferreira<sup>1</sup>, Thyago H. S. Cardoso<sup>2</sup>, Edson M.A. Silva<sup>3</sup>, Nitin K. Saksena<sup>4</sup> and  Wael M. Rabeh<sup>1</sup>

<sup>1</sup>Science Division, New York University Abu Dhabi, PO Box 129188, Abu Dhabi, United Arab Emirates; <sup>2</sup>G42 Healthcare, Omics Excellence Center, Masdar City, Abu Dhabi, United Arab Emirates; <sup>3</sup>Science Division, Universidade Federal de Minas Gerais, Belo Horizonte, Minas Gerais, Brazil; <sup>4</sup>IHES, Victoria University, Footscray Campus, Melbourne, Victoria, Australia

**Correspondence:** Wael M. Rabeh ([wael.rabeh@nyu.edu](mailto:wael.rabeh@nyu.edu))



Coronaviruses have been responsible for multiple challenging global pandemics, including coronavirus disease 2019 (COVID-19), which is caused by severe acute respiratory syndrome coronavirus 2 (SARS-CoV-2). Papain-like protease (PLpro), one of two cysteine proteases responsible for the maturation and infectivity of SARS-CoV-2, processes and liberates functional proteins from the viral polyproteins and cleaves ubiquitin and ISG15 modifications to inhibit innate immune sensing. Consequently, PLpro is an attractive target for developing COVID-19 therapies. PLpro contains a zinc-finger domain important for substrate binding and structural stability. However, the impact of metal ions on the activity and biophysical properties of SARS-CoV-2 PLpro has not been comprehensively studied. Here, we assessed the impacts of metal ions on the catalytic activity of PLpro. Zinc had the largest inhibitory effect on PLpro, followed by manganese. Calcium, magnesium, and iron had smaller or no effects on PLpro activity. EDTA at a concentration of 0.5 mM was essential for PLpro activity, likely by chelating trace metals that inhibit PLpro.  $IC_{50}$  values for  $ZnCl_2$ ,  $ZnSO_4$ , and  $MnCl_2$  of  $0.42 \pm 0.02$  mM,  $0.35 \pm 0.01$  mM, and  $2.6 \pm 0.3$  mM were obtained in the presence of 0.5 mM EDTA; in the absence of EDTA, the estimated  $IC_{50}$  of  $ZnCl_2$  was 14  $\mu$ M. Tryptophan intrinsic fluorescence analysis confirmed the binding of zinc and manganese to PLpro, and differential scanning calorimetry revealed that zinc but not manganese reduced  $\Delta H_{cal}$  of PLpro. The results of this study provide a reference for further work targeting PLpro to prevent and treat COVID-19.

## Introduction

Since its discovery in late 2019, coronavirus disease 19 (COVID-19) has infected over a half billion people and caused more than six million deaths [1]. Severe acute respiratory syndrome coronavirus 2 (SARS-CoV-2) is the novel coronavirus responsible for COVID-19 [2,3]. Human coronaviruses cause illnesses ranging from the common cold to highly pathogenic respiratory diseases, including respiratory disease outbreaks in 2002 and 2012 linked to SARS-CoV and Middle East respiratory syndrome coronavirus (MERS-CoV), respectively [4–6]. Due to the high transmission efficiency of SARS-CoV-2, the COVID-19 outbreak quickly evolved from an epidemic to a pandemic in early 2020 and continues to affect lives worldwide [7].

SARS-CoV-2 is an enveloped virus belonging to the genus  $\beta$ -coronavirus and has a positive-sense, single-stranded RNA genome of  $\sim 30$  kb [8]. The genome of SARS-CoV-2 has high similarity with those of other  $\beta$ -coronaviruses and shares  $\sim 80\%$  of its genome with SARS-CoV and 50% with MERS-CoV. After the coronavirus spike (S) protein specifically binds to the outside of the host cell, the viral genomic RNA enters the cell and is translated via two open reading frames (ORFs), ORF1a

Received: 16 July 2022  
 Revised: 26 September 2022  
 Accepted: 7 October 2022

Accepted Manuscript online:  
 7 October 2022  
 Version of Record published:  
 21 October 2022

and ORF1b, to produce polyproteins containing non-structural proteins (nsps) [6,8]. The polyproteins translated from ORF1a and ORF1b, pp1a and pp1ab, are cleaved by the cysteine proteases 3-chymotrypsin-like cysteine protease (3CLpro) and papain-like protease (PLpro), which are encoded by *nsp5* and *nsp3*, respectively. PLpro cleaves sites between nsp1 and 2, nsp2 and 3, and nsp3 and 4, while 3CLpro processes the other 11 sites between the remaining nsps, resulting in a total of 16 nsps [6,8–10]. These nsps then assemble to form the viral replication and transcription complex on the host cell membrane.

In addition to its role in viral maturation, PLpro inhibits the host immune response, further increasing its attractiveness as a drug target [6,10]. PLpros from various coronaviruses have been shown to antagonize the type I interferon (IFN) pathway by inactivating different components of the pathway [11–13]. For example, PLpro inhibits the phosphorylation and nuclear translocation of IRF-3 to disrupt the activation of type I IFN responses [12,13]. In addition, PLpro is a deubiquitinating enzyme that cleaves the LXGG sequence found in the C-terminal tail of ubiquitin and the ubiquitin-like modification ISG15 [13,14]. PLpro cleaves both types of modifications to inhibit innate immune sensing [9]. PLpro's ability to remove ubiquitin and ISG15 modifications impedes the host's ability to tag and degrade foreign proteins, including viral proteins [14,15]. Targeting conserved coronavirus proteins like SARS-CoV-2 PLpro, which shares structural and functional similarities with the PLpros of other human coronaviruses such as SARS-CoV and MERS-CoV, has the potential to treat multiple coronavirus strains [16,17]. To design effective treatment strategies targeting PLpro, an investigation of the biochemical and biophysical properties of PLpro is required to identify key similarities and differences between coronaviruses.

Like other human deubiquitinating enzymes belonging to the ubiquitin-specific protease family, including SARS-CoV PLpro, the tertiary structure of SARS-CoV-2 PLpro resembles a hand with four domains: the fingers, palm, thumb, and Ub1 binding domains [9,18]. The catalytic site is located between the palm and thumb domains and comprises the conserved catalytic residues Cys111, His272, and Asp286 [18,19]. The Ub1 binding domain binds the C-terminus of ubiquitin or ISG15, which contains an LXGG cleavage site that enters the catalytic site [19,20]. The catalytic site also cleaves viral proteins containing the LXGG sequence to facilitate the maturation of the viral replicase complex. The fingers domain cradles the ubiquitin in the palm domain once it binds to PLpro and is necessary for structural stability [19]. The fingers domain contains a labile zinc finger ribbon motif in which a  $Zn^{2+}$  ion is tetrahedrally complexed with four cysteines [21–23]. Substituting these zinc-binding cysteines with alanine results in loss of function, emphasizing the importance of this domain to the function and structure of PLpro [24].

Zinc finger domains are a common feature of antiviral proteins, and FDA-approved zinc-ejecting drugs that target this domain are currently on the market [21]. These zinc-ejectors disrupt the zinc-cysteine tetrahedral complex by binding to the cysteine, thus releasing the zinc. However, a molecular dynamics study of PLpro revealed that the zinc finger domain is highly flexible, suggesting that this region may be a poor drug target because it is too dynamic for small-molecule drugs to bind tightly [25]. Nonetheless, the zinc-ejector drugs disulfiram and ebselen destabilize PLpro, thereby reducing its catalytic activity, and could be used in tandem with other antiviral drugs as part of a multi-target approach to treat COVID-19 [21,26,27].

Despite the essential role of zinc in the structure of PLpro, studies of the effects of metal ions on the biochemical properties of PLpro have been limited to analyses of kinetics and thermodynamic stability, and none of these studies has examined the impact of metal chelators such as EDTA on catalytic function [5,28,29]. Here, we present a detailed analysis of the abilities of different metal ions, including zinc, magnesium, manganese, calcium, and iron, to bind and inhibit PLpro. We also analyzed the impact of EDTA on PLpro activity and divalent metal ion binding. The results revealed that zinc had the most significant inhibitory effect on PLpro, followed by manganese. The presence of EDTA was essential for PLpro activity, likely by chelating trace metal ions that inhibit PLpro. The binding of zinc and manganese to PLpro was confirmed by tryptophan intrinsic fluorescence analysis; however, differential scanning calorimetry revealed that zinc, but not manganese, reduced  $\Delta H_{cal}$  of PLpro. The results of this study provide a durable framework for future efforts to target PLpro to successfully prevent and treat SARS-CoV-2 infection.

## Results

### The effects of metal ions and EDTA on the catalytic activity of PLpro

The effects of five metal ions on the catalytic activity of SARS-CoV-2 were evaluated: zinc, magnesium, manganese, calcium, and iron. The activity of PLpro was determined by assaying the proteolytic digestion of the

fluorogenic peptide substrate CBZ-LRGG-AMC, where CBZ (carbobenzoxy) is a quencher for the AMC (7-amino-4-methyl coumarin) fluorescent probe [29,30]. Following previous studies, PLpro activity was measured in 50 mM HEPES pH 7.5, 0.5 mM EDTA, and 0.5 mM TCEP at a fixed peptide substrate concentration of 135  $\mu$ M [31–33]. PLpro had very little activity in 50 mM HEPES pH 7.5 and 0.5 mM TCEP, whereas activity recovered upon the addition of EDTA. Titration with different concentrations of EDTA indicated that 0.5 mM EDTA was optimal for PLpro activity, consistent with a previous report [33]. Therefore, 0.5 mM EDTA was included in all PLpro assays.

In the initial screen, chloride salts of all metals plus zinc sulfate were used at a concentration of 1 mM. Adding 1 mM  $\text{ZnCl}_2$  or  $\text{ZnSO}_4$  resulted in almost complete inhibition of PLpro, whereas 1 mM  $\text{MnCl}_2$  or  $\text{CaCl}_2$  reduced PLpro activity by  $\sim$ 40% (Figure 1a). Neither 1 mM  $\text{MgCl}_2$  nor 1 mM  $\text{FeCl}_2$  affected the activity of PLpro significantly (Figure 1a). The effects of zinc, manganese, and calcium on SARS-CoV-2 PLpro activity were further investigated by determining their  $\text{IC}_{50}$ s. The calculated  $\text{IC}_{50}$ s of the metal ions are dependent on the concentrations of PLpro and the peptide substrate, which were 0.5  $\mu$ M and 135  $\mu$ M in the assay, respectively. Zinc exhibited the strongest inhibitory effect on the enzymatic activity of PLpro (Figure 1b,c). The

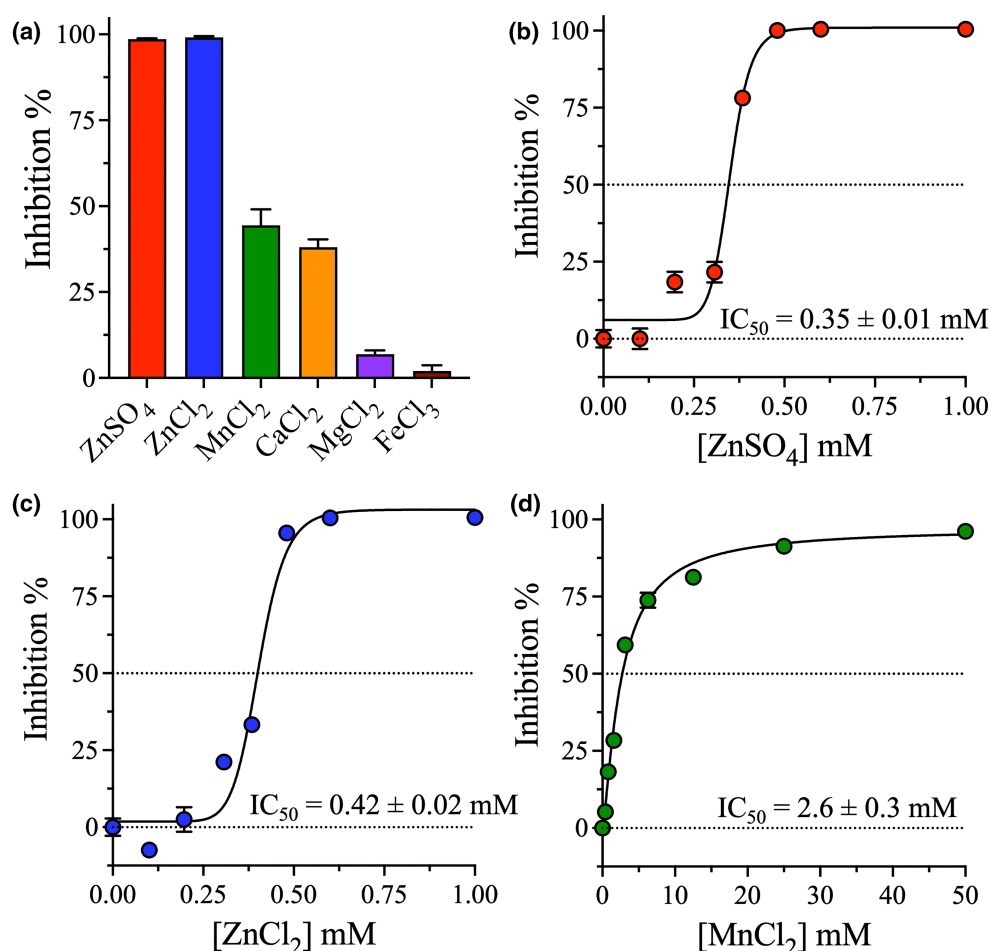


**Figure 1. Effect of metal ions on the activity of PLpro.**

(a) Bar plot of the percent inhibition of PLpro in the presence of zinc sulfate and chloride salts of zinc, magnesium, manganese, calcium, and iron at a metal ion concentration of 1 mM. The PLpro assay was performed in 50 mM HEPES pH 7.5, 0.5 mM EDTA, and 0.5 mM TCEP at a fixed peptide substrate concentration of 135  $\mu$ M and a PLpro enzyme concentration of 0.5  $\mu$ M. The percent inhibition was determined by comparing the rate in the presence and absence of metal ions. (b–d) Determination of the  $\text{IC}_{50}$  values of the metal ions that reduced the catalytic activity of PLpro in the initial screen. The  $\text{IC}_{50}$  of calcium could not be determined because 50% inhibition was not reached at a calcium chloride concentration of 100 mM. Data points are means  $\pm$  S.D. of triplicate determinations.

calculated  $IC_{50}$  values for  $ZnCl_2$ ,  $ZnSO_4$ , and  $MnCl_2$  were  $0.42 \pm 0.02$  mM,  $0.35 \pm 0.01$  mM, and  $2.6 \pm 0.3$  mM, respectively (Figure 1d). Although 1 mM  $CaCl_2$  reduced PLpro activity by  $\sim 40\%$  in the initial screen, increasing the calcium concentration to 100 mM only reduced PLpro activity by  $\sim 70\%$ ; therefore, an  $IC_{50}$  value could not be calculated for calcium.

Since the presence of EDTA in the enzyme assay buffer increased the activity of PLpro, the effect of EDTA on the  $IC_{50}$  of zinc was investigated. The  $IC_{50}$  values for zinc ion reported above were slightly lower than the EDTA concentration of 0.5 mM included in the PLpro enzyme assay buffer. To estimate the inhibitory effect of zinc in the absence of EDTA, the  $IC_{50}$  of  $ZnCl_2$  was determined at different concentrations of EDTA: 0.1 mM, 0.5 mM, 1.0 mM, 2.5 mM, 5.0 mM and 10.0 mM EDTA (Figure 2a,b). The  $IC_{50}$  of zinc increased linearly as the concentration of EDTA increased (Figure 2c). Extrapolation of the linear fit of the  $IC_{50}$  of  $ZnCl_2$  to the y-intercept gave an estimated  $IC_{50}$  value of  $14 \mu\text{M}$   $ZnCl_2$  in the absence of EDTA (Figure 2c).

## Pattern of PLpro inhibition by metal ions

To further investigate the inhibitory effects of zinc and manganese on PLpro activity, initial velocity patterns were obtained in the presence of varying concentrations of the peptide substrate and different fixed concentrations of the metal salts in the presence of 0.5 mM EDTA. The concentration of the peptide substrate was varied at 55, 110, 250, and 800  $\mu\text{M}$  in the presence of 1.0, 1.5, 2.5, or 6.0 mM  $MnCl_2$  (Figure 3). Manganese yielded a mixed inhibition pattern against PLpro with an inhibition constant ( $K_i$ ) of  $1.5 \pm 0.4$  mM. A similar inhibition study was performed on the zinc salts; however, due to the sharp inhibition window observed during the  $IC_{50}$  calculations, mechanistic characterization of zinc inhibition of PLpro was not experimentally feasible, and we could not accurately estimate the inhibition patterns.

## Evaluation of the binding affinity of PLpro for metal ions based on tryptophan fluorescence

SARS-CoV-2 PLpro contains two tryptophan residues (Trp-96 and Trp-109) and 24 tyrosine residues. The two tryptophan residues are located near the active site of PLpro, while the tyrosine residues are spread throughout the protease structure. To estimate the binding affinity of PLpro for metal ions, the change in tryptophan fluorescence upon titration with  $ZnSO_4$ ,  $ZnCl_2$ , or  $MnCl_2$  was measured. The tryptophan emission scans of PLpro were collected at emission wavelengths ( $\lambda_{em}$ ) from 300 nm to 450 nm using an excitation wavelength ( $\lambda_{ex}$ ) of 290 nm to minimize tyrosine emission (Figure 4a–c). Metal ion titration resulted in changes in fluorescence intensity in the emission spectra in a metal concentration-dependent manner; however, the emission profiles

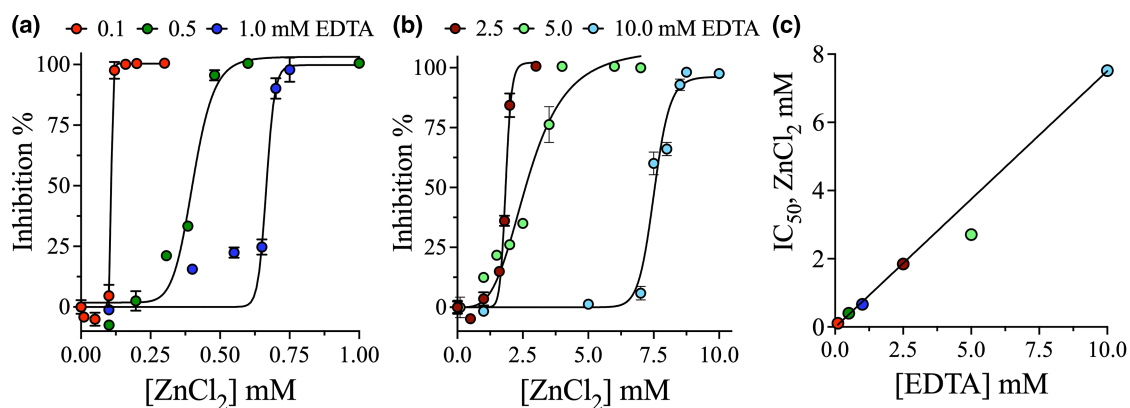


**Figure 2. Effect of EDTA on the  $IC_{50}$ s of metal ions.**

(a and b) The  $IC_{50}$  profiles of  $ZnCl_2$  against PLpro were determined in the presence of 0.1 mM, 1.0 mM, 2.5 mM, 5.0 mM, and 10.0 mM EDTA. The peptide substrate concentration and reaction conditions were similar to those in Figure 1. The  $IC_{50}$  was determined at the mid-transition point, giving values of  $0.11 \pm 0.02$  mM,  $0.40 \pm 0.02$  mM,  $0.67 \pm 0.01$  mM,  $1.80 \pm 0.02$  mM,  $2.90 \pm 0.01$  mM, and  $7.50 \pm 0.15$  mM at EDTA concentrations of 0.1 mM, 1 mM, 2.5 mM, 5 mM, and 10 mM, respectively. (c) The plot of the  $IC_{50}$  of  $ZnCl_2$  versus EDTA concentration was linear. Extrapolation of the  $IC_{50}$  value to 0 mM EDTA from the linear fit gave a value of  $14 \mu\text{M}$  for  $ZnCl_2$ . Data points are means  $\pm$  S.D. of triplicate determinations.

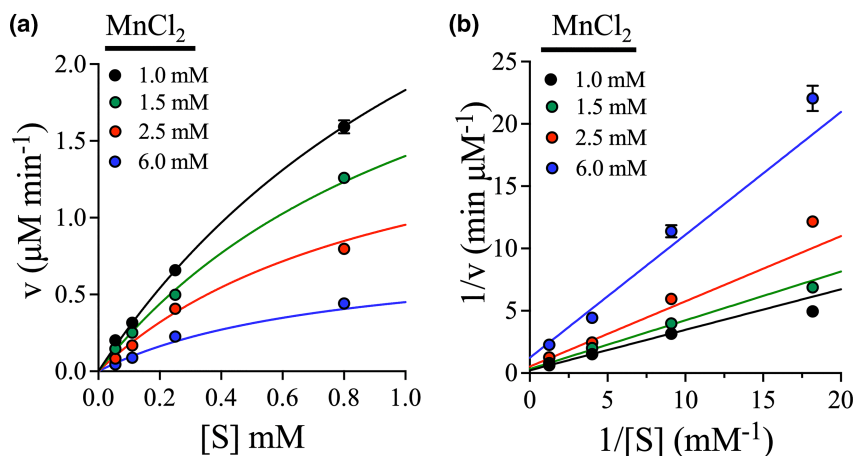


**Figure 3. Inhibition pattern of PLpro by manganese.**

(a) Michaelis–Menten fit graph and (b) Lineweaver–Burk graph of the non-competitive inhibition of PLpro by  $\text{MnCl}_2$ . Points are experimental data, and lines represent the best fit of the data. The assay was performed in 50 mM HEPES pH 7.5, 0.5 mM EDTA, and 0.5 mM TCEP. The concentration of the peptide substrate was varied at 55  $\mu\text{M}$ , 75  $\mu\text{M}$ , 250  $\mu\text{M}$ , and 800  $\mu\text{M}$ . The lines represent increasing concentrations of manganese chloride at 1 mM, 1.5 mM, 2.5 mM, and 6 mM. The calculated  $K_i$  for manganese chloride is  $1.5 \pm 0.4$  mM. Data points are means  $\pm$  S.D. of triplicate determinations.

for zinc and manganese did not show a notable blueshift or redshift. In all spectra, the maximum tryptophan fluorescence intensity occurred at an emission wavelength ( $\lambda_{\text{max}}$ ) of 342 nm (Figure 4a–c).

After adding 2  $\mu\text{M}$   $\text{ZnSO}_4$  or  $\text{ZnCl}_2$ , the intensity of the intrinsic tryptophan fluorescence signal of PLpro increased sharply by 20% and 60%, respectively, compared with the enzyme in the absence of zinc (Figure 4a, b). Further increasing the zinc concentration beyond 2  $\mu\text{M}$  resulted in quenching of fluorescence below the fluorescence intensity of the free enzyme. Similarly, titration of PLpro with  $\text{MnCl}_2$  initially increased the emission signal, with a maximum increase in 30% at 50  $\mu\text{M}$   $\text{MnCl}_2$  (Figure 4c). Further increasing the manganese concentration to 5 mM resulted in quenching, although the fluorescence intensity remained higher than that of the free enzyme (Figure 4c), in contrast with the titration of PLpro with high concentrations of  $\text{ZnCl}_2$  and  $\text{ZnSO}_4$ .

To estimate the binding affinity constant ( $K_D$ ) of metal ions to PLpro, the change in the tryptophan fluorescence signal was plotted as a function of the metal ion concentration, and the graphs were fit to a one-site binding model using GraphPad Prism 9 (Figures 4d–f). The effect of protein dilution upon the addition of the metal ion was considered, and a background fluorescence emission scan was obtained in parallel with the ion titration scans by adding buffer only. The reduction in fluorescence intensity due to the addition of buffer was insignificant compared with the quenching of the PLpro signal due to metal ion titration. As expected, the  $K_D$  values of  $\text{ZnSO}_4$  ( $0.48 \pm 0.21$  mM) and  $\text{ZnCl}_2$  ( $0.27 \pm 0.17$  mM) were 10-fold lower than that of  $\text{MnCl}_2$  ( $2.74 \pm 0.60$  mM), indicating a higher binding affinity of PLpro for zinc compared with manganese.

### Effects of metal ions and EDTA on the thermodynamic stability of PLpro

The thermodynamic stability of PLpro was first assessed in the absence of EDTA by DSC in the presence and absence of 0.25 mM or 0.5 mM  $\text{ZnSO}_4$ ,  $\text{ZnCl}_2$ , or  $\text{MnCl}_2$  in 50 mM HEPES pH 7.0 and 0.5 mM TCEP (Figure 5a,b). The temperature was ramped from 15°C to 75°C at a scan rate of 1°C/min to acquire the thermal unfolding transitions. The melting temperature ( $T_m$ ) was calculated at the apex of the melting peak, and the calorimetric enthalpy ( $\Delta H_{\text{cal}}$ ) was determined from the area under the thermographic peak. The DSC scan of PLpro in the absence of metal salts exhibited a two-phase transition with a late shoulder peak (Figure 5a). The overall shape of the thermogram was the same in the presence of  $\text{ZnSO}_4$ , except that the shoulder peak was less prominent (Figure 5a).  $T_m$  decreased from  $44.2 \pm 0.1^\circ\text{C}$  in the absence of  $\text{ZnSO}_4$  to  $35.3 \pm 0.4^\circ\text{C}$  at 0.25 mM  $\text{ZnSO}_4$  and  $34.3 \pm 0.3^\circ\text{C}$  at 0.5 mM  $\text{ZnSO}_4$  (Figure 5d).  $\Delta H_{\text{cal}}$  decreased slightly from  $1476 \pm 113$  kJ/mol in the absence of  $\text{ZnSO}_4$  to  $1302 \pm 30$  kJ/mol at 0.25 mM  $\text{ZnSO}_4$  (Figure 5f) but exhibited a larger drop to  $540 \pm 14$  kJ/mol at 0.5 mM  $\text{ZnSO}_4$  (Figure 5f). Adding 0.25 mM  $\text{ZnSO}_4$  marginally decreased  $\Delta H_{\text{cal}}$  by 174 kJ/mol, while a larger decrease in 936 kJ/mol was observed upon the addition of 0.5 mM  $\text{ZnSO}_4$ .

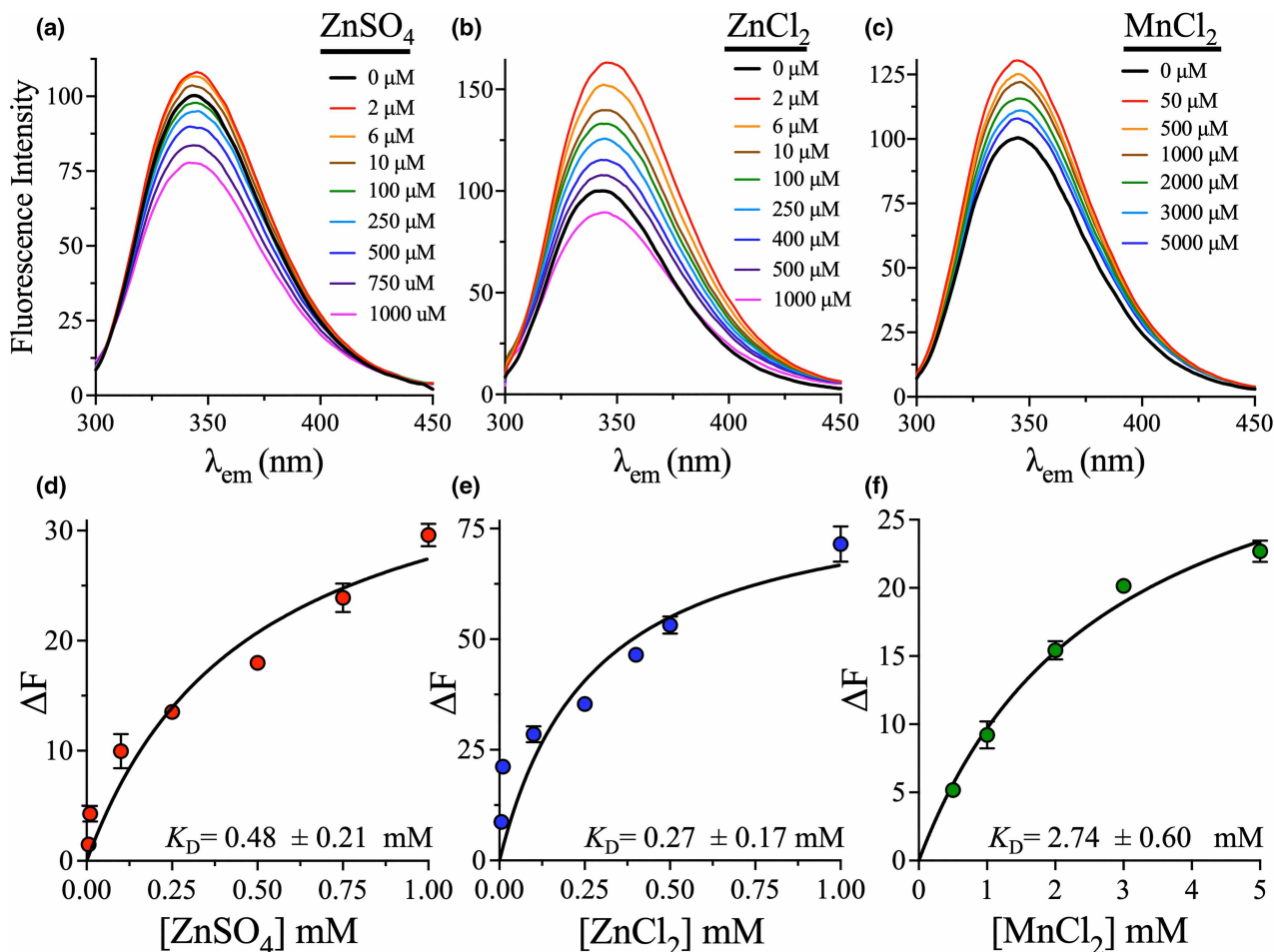


**Figure 4. Tryptophan fluorescence measurement for the determination of metal ion binding affinity.**

(a–c) Intrinsic tryptophan fluorescence scans of PLpro in the presence of increasing concentrations of metal ions with excitation at 290 nm. The emission of PLpro initially increased with the addition of ZnSO<sub>4</sub>, ZnCl<sub>2</sub>, and MnCl<sub>2</sub>. Upon titration with higher concentrations of the metal ions, quenching of the tryptophan fluorescence signal was observed. (d and e) Change in fluorescence intensity at the maximum emission wavelength ( $\lambda_{em}$ ) of 342 nm as a function of metal ion concentration. The data were fit to a one-site specific binding model to determine the  $K_D$  values for ZnSO<sub>4</sub>, ZnCl<sub>2</sub>, and MnCl<sub>2</sub>.

A similar thermodynamic destabilization effect was observed for ZnCl<sub>2</sub>, with a major two-phase transition (Figure 5a). The  $T_m$  values for the early and late thermographic transitions ( $T_{m1}$  and  $T_{m2}$ ) decreased by  $\sim 10^\circ\text{C}$  in the presence of 0.25 mM and 0.5 mM ZnCl<sub>2</sub> (Figure 5d,e). Similar to the impact of ZnSO<sub>4</sub>,  $\Delta H_{cal}$  decreased slightly from  $1476 \pm 113$  kJ/mol in the absence of ZnCl<sub>2</sub> to  $1149 \pm 122$  kJ/mol in the presence of 0.25 mM ZnCl<sub>2</sub>, a decrease in 327 kJ/mol (Figure 5f). The addition of 0.5 mM ZnCl<sub>2</sub> resulted in an even larger drop to  $634 \pm 41$  kJ/mol, a decrease in 842 kJ/mol.

The DSC thermograms of PLpro in the presence of MnCl<sub>2</sub> also exhibited a two-phase transition. Adding 0.25 mM MnCl<sub>2</sub> shifted the thermographic peak to lower temperatures but did not significantly affect the peak height (Figure 5c). The  $T_{m1}$  and  $T_{m2}$  values for the first and second transitions decreased by  $13^\circ\text{C}$  and  $9^\circ\text{C}$ , respectively, upon adding 0.25 mM MnCl<sub>2</sub> (Figure 5d,e). The  $\Delta H_{cal}$  values were identical in the absence or presence of 0.25 mM MnCl<sub>2</sub> (Figure 5f). Increasing the concentration of MnCl<sub>2</sub> to 0.5 mM did not further decrease  $T_{m1}$  and  $T_{m2}$  compared with 0.25 mM MnCl<sub>2</sub>. However, a drop in  $\Delta H_{cal}$  of 490 kJ/mol was observed in the presence of 0.5 mM MnCl<sub>2</sub>, whereas no change in  $\Delta H_{cal}$  was observed upon adding 0.25 mM MnCl<sub>2</sub>.

Next, the impact of EDTA on the binding of zinc to PLpro was assessed. First, the thermodynamic stability of PLpro was assessed in the free enzyme state in the absence and presence of equal concentrations of 0.5 mM

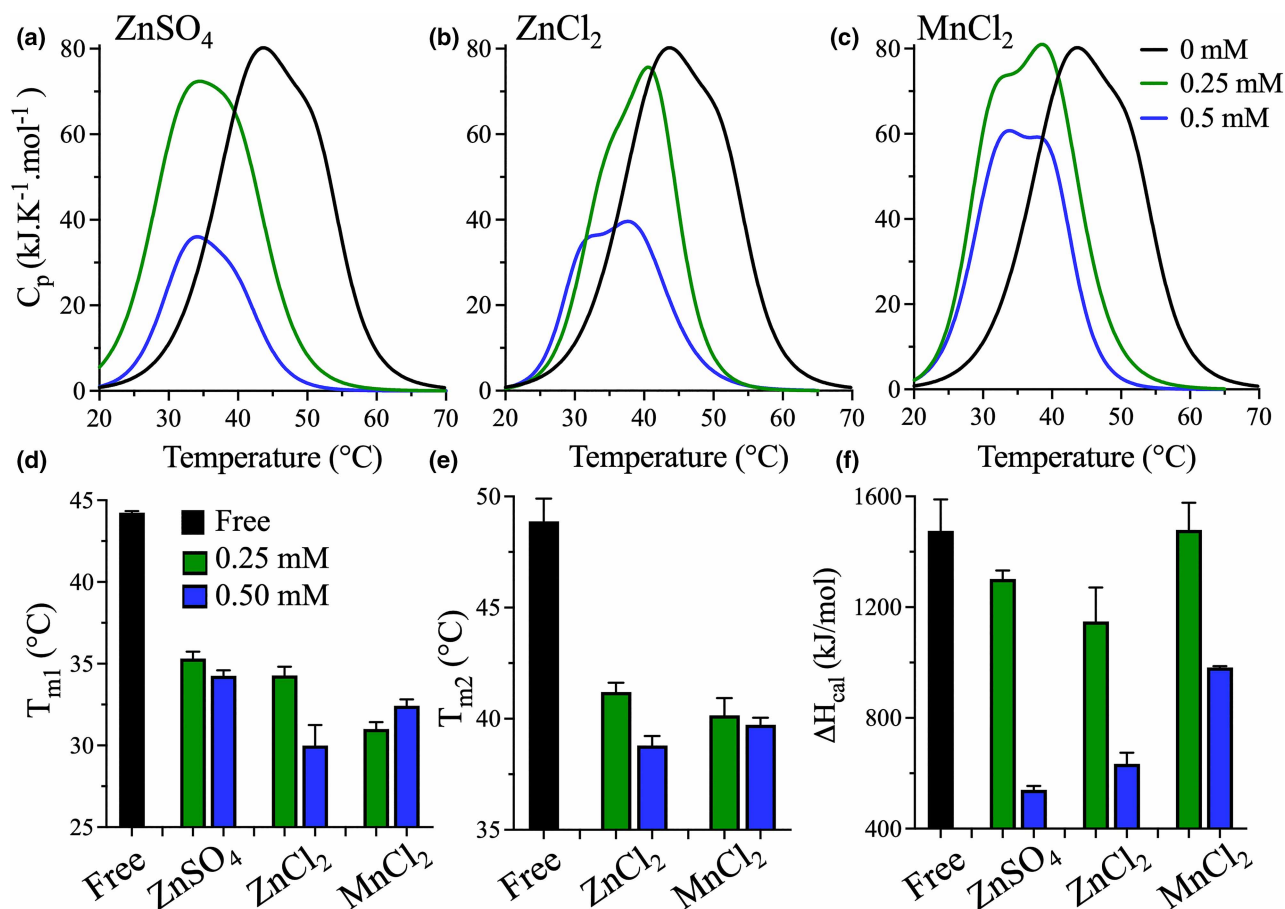


**Figure 5. Effect of metal ions on the thermodynamic stability of PLpro.**

(a–c) DSC thermal scans of PLpro in the absence (black) and presence of 0.25 mM (green) or 0.5 mM (blue) zinc sulfate, zinc chloride, or manganese chloride. The temperature was increased from 20°C to 85°C at scanning rate of 1°C/min in buffer containing 50 mM HEPES pH 7.0 and 0.5 TCEP. (d and e) Bar plots of the  $T_{m1}$  and  $T_{m2}$  values calculated from the midpoints of the thermal transitions of the DSC scans. The addition of 0.25 mM metal salt reduced  $T_m$  compared with its absence (black); however, further increasing the concentration to 0.50 mM (blue) did not change the  $T_m$  value of PLpro. (f) Bar plots of  $\Delta H_{\text{cal}}$  of PLpro at different concentrations of zinc and manganese salts. The addition of 0.25 mM (green) zinc slightly decreased the  $\Delta H_{\text{cal}}$  value of PLpro, whereas manganese did not affect  $\Delta H_{\text{cal}}$ . Increasing the concentration of salt to 0.50 mM (blue) greatly reduced  $\Delta H_{\text{cal}}$ , indicating a change in the overall bonding interactions of the protein structure. Increasing the concentration of zinc decreased the  $\Delta H_{\text{cal}}$  of PLpro more than increasing the concentration of manganese to 0.5 mM. Data points are means  $\pm$  S.D. of triplicate determinations.

EDTA and 0.5 mM  $\text{ZnSO}_4$ . Under the latter conditions, effectively none of the zinc ions were available for binding to PLpro. The overall shapes of the two DSC thermograms were similar, except that the small shoulder of the late transition that was present in the absence of EDTA disappeared in the presence of equal concentrations of EDTA and  $\text{ZnSO}_4$  (Figure 6a).  $T_m$  decreased by 2°C in the presence of equal concentrations of EDTA and  $\text{ZnSO}_4$  (Figure 6d), whereas  $\Delta H_{\text{cal}}$  was similar under the two conditions (Figure 6e).

Similar DSC analyses were performed to assess the effects of 0.25 mM and 0.5 mM  $\text{ZnSO}_4$  on the thermodynamic stability of PLpro in the presence or absence of EDTA. In the absence of EDTA, only 0.25 mM and 0.5 mM  $\text{ZnSO}_4$  were included. In contrast, 0.75 mM and 1.0 mM  $\text{ZnSO}_4$  were added in the presence of 0.5 mM EDTA to obtain unchelated zinc ion concentrations of 0.25 mM and 0.5 mM, respectively. The shapes of the DSC thermographic peaks for the 0.25 mM and 0.5 mM  $\text{ZnSO}_4$  states were similar in the presence or absence of 0.5 mM EDTA (Figure 6b,c).  $T_m$  was  $\sim 34.5^{\circ}\text{C}$  in the presence of 0.25 mM  $\text{ZnSO}_4$  regardless of the presence of 0.5 mM EDTA, corresponding to a decrease in 9°C compared with the  $T_m$  of free PLpro (Figure 6d). However,  $T_m$  did not decrease further upon increasing the  $\text{ZnSO}_4$  concentration to 0.5 mM. In addition,  $\Delta H_{\text{cal}}$  of PLpro decreased slightly upon adding 0.25 mM  $\text{ZnSO}_4$ , with decreases of 174 kJ/mol and 283 kJ/mol in the absence or

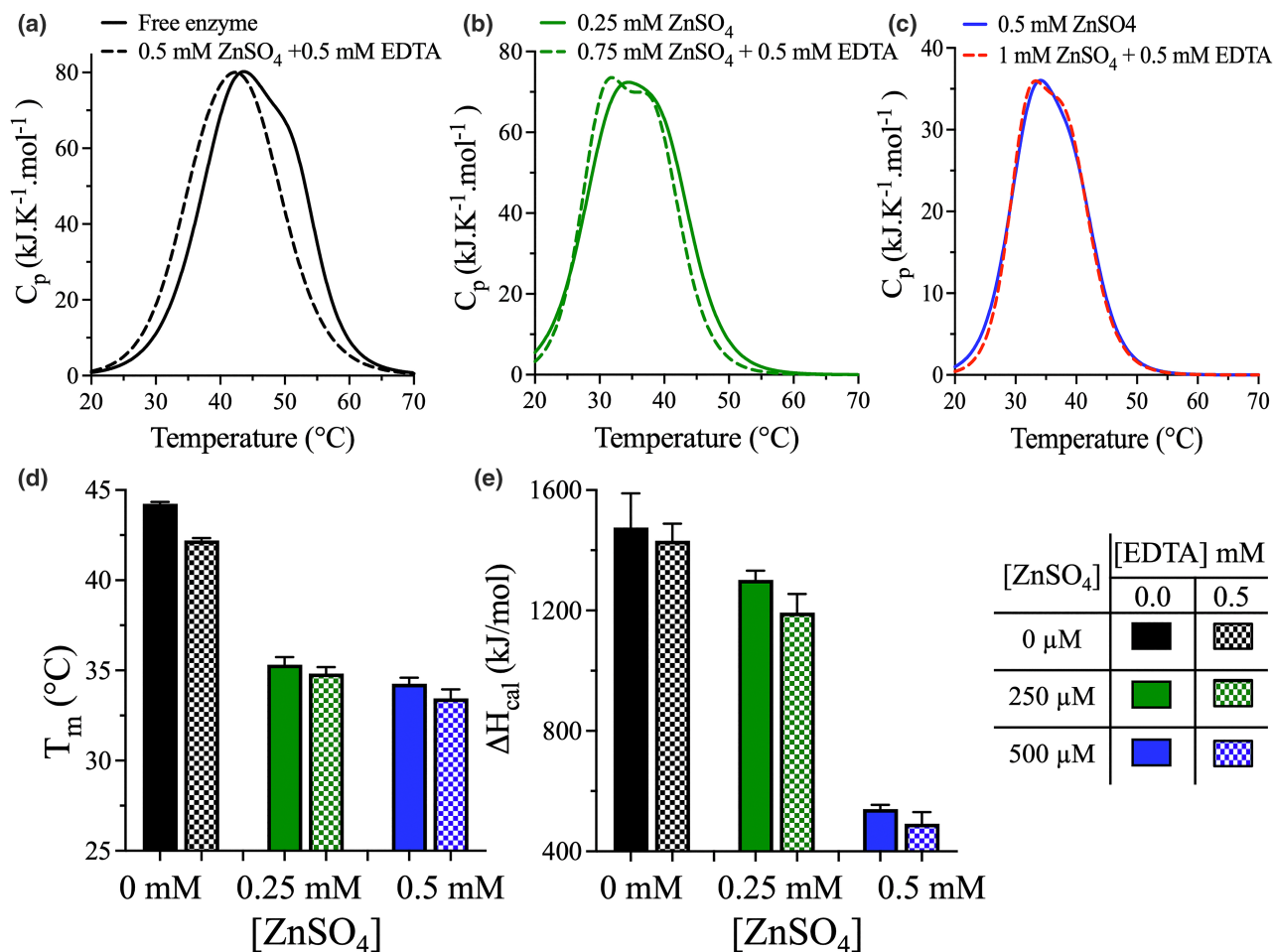


**Figure 6. Effect of EDTA on the thermodynamic stability of PLpro in the presence of zinc sulfate.**

(a) DSC thermal scans of PLpro in the free enzyme (black) state. In the absence of EDTA, (solid line), the DSC scan of PLpro was collected for the free enzyme. In the presence of 0.5 mM EDTA (dashed line), an equivalent concentration of 0.5 mM ZnSO<sub>4</sub> was added. The DSC scanning conditions and parameters were similar to those in Figure 3. (b) DSC scans of PLpro in the presence of 0.25 mM ZnSO<sub>4</sub> state (green). In the absence of EDTA (solid line), 0.25 mM ZnSO<sub>4</sub> was included; however, in the presence of 0.5 mM EDTA (dashed line), 0.75 mM ZnSO<sub>4</sub> was added. (c) DSC scans of PLpro in the presence of 0.5 mM ZnSO<sub>4</sub>. In the absence of EDTA (solid blue line), 0.5 mM of ZnSO<sub>4</sub> was included; however, in the presence of 0.5 mM EDTA (dashed red line), 1 mM ZnSO<sub>4</sub> was added. (d) Bar plot of  $T_m$  values for PLpro at different concentrations of ZnSO<sub>4</sub> in the presence (solid bars) and absence (checkered bars) of 0.5 mM EDTA. The presence of EDTA did not affect the  $T_m$  of PLpro when an equivalent concentration of ZnSO<sub>4</sub> was present. Similar to the measurements in Figure 5, the presence of 0.25 mM ZnSO<sub>4</sub> reduced the  $T_m$  of PLpro; however, increasing the concentration of ZnSO<sub>4</sub> to 0.5 mM did not change the  $T_m$  of PLpro regardless of the presence or absence of EDTA. (e) Bar plots of  $\Delta H_{cal}$  of PLpro at different concentrations of ZnSO<sub>4</sub> in the presence (solid bars) and absence (checkered bars) of 0.5 mM EDTA. The addition of EDTA did not alter the  $\Delta H_{cal}$  values of PLpro when an equivalent concentration of ZnSO<sub>4</sub> was present. Data points are means  $\pm$  S.D. of triplicate determinations.

presence of 0.5 mM EDTA, respectively (Figure 6e). However, upon adding 0.5 mM ZnSO<sub>4</sub>,  $\Delta H_{cal}$  decreased significantly by 936 kJ/mol and 984 kJ/mol in the absence or presence of 0.5 mM EDTA, respectively.

### Effects of metal ions on the structural integrity of PLpro

In the presence of metal ions, the  $T_m$  of PLpro decreased by  $\sim 10^\circ\text{C}$ , indicating a decrease in thermodynamic stability. To confirm that the inhibition of PLpro by zinc or manganese was not a result of denaturation of the protease, the effects of metal ions on the structural integrity of PLpro were assessed by far-UV CD spectroscopy. First, CD spectra of PLpro in the native and denatured states were acquired at 25°C and after incubation for 30 min at



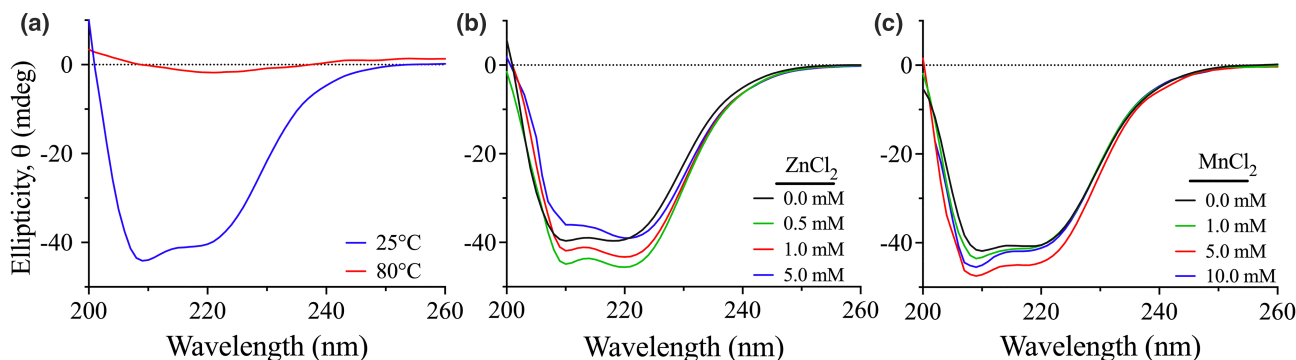


**Figure 7. Far-UV circular dichroism scans of PLpro.**

Far-UV CD spectra of PLpro were collected from 260 to 200 nm. (a) The native (blue) and denatured (red) states of PLpro were collected at 25°C and after incubation for 30 min at 80°C, respectively. (b and c) Far-UV CD spectra of native PLpro collected at 25°C in the absence (black) and presence of different concentrations of zinc and manganese metal ions. The concentration of ZnCl<sub>2</sub> was varied at 0.5 mM (green), 1.0 mM (red), and 5.0 mM (green), while the concentration of MnCl<sub>2</sub> was varied at 1.0 mM (green), 5.0 mM (red), and 10.0 mM (green). Each spectrum was corrected for the buffer background and is the average of five CD scans.

80°C, respectively (Figure 7a). The CD spectra were collected from 200 nm to 260 nm, and each spectrum was the average of five CD scans. The CD spectrum of PLpro in the native state showed two ellipticity minima at 208 and 222 nm, consistent with mixed  $\alpha$ -helical and  $\beta$ -sheet structures [5,34]. In the denatured state, a total loss of the secondary structural elements of PLpro was observed, as indicated by the reduction in its ellipticity.

Next, far-UV CD spectra of PLpro were collected in the presence of different concentrations of ZnCl<sub>2</sub> or MnCl<sub>2</sub> at 25°C (Figure 7b,c). The addition of either metal ion induced structural changes in SARS-CoV-2 PLpro, but the folded state was maintained. The addition of 0.5 mM and 1.0 mM ZnCl<sub>2</sub> increased the negative ellipticity of PLpro at 208 nm by 11% and 3%, respectively, compared with the enzyme in the absence of zinc (Figure 7b). The increase in the negative ellipticity of PLpro in the presence of zinc indicates an enhancement of its secondary structural content. However, the CD spectrum of PLpro in the presence of 5.0 mM ZnCl<sub>2</sub> was similar to that of PLpro in the absence of metal ions. Thus, depending on its concentration, the presence of zinc either enhanced or had no effect on the structural integrity of PLpro.

Similarly, the addition of manganese increased the negative ellipticity of PLpro by 6%, 16%, and 13% in the presence of 1.0 mM, 5.0 mM, and 10.0 mM MnCl<sub>2</sub>, respectively (Figure 7c). Thus, both manganese and zinc enhanced the structural integrity of PLpro. The metal ion concentrations used in CD spectroscopy were higher than the  $K_D$  values of 0.27 mM and 2.74 mM for ZnCl<sub>2</sub> and MnCl<sub>2</sub> from tryptophan fluorescence measurements, respectively; therefore, the observed inhibition of PLpro by zinc and manganese reflects the loss of enzymatic activity rather than denaturation of the protease.

## Interactome of PLpro with host proteins and the relevance of Zn<sup>2+</sup> and Mn<sup>2+</sup>

We considered only hub proteins and those human proteins directly connected to the hub proteins in the interactome analysis. Hub proteins have the most connections with other human proteins in the network and best represent the overall functional relevance of the proteins in the network. Human proteins associated with SARS-CoV-2 PLpro were classified as Level 1 or Level 2 (Figure 8). Level 1 human proteins are in the immediate vicinity of or directly connected to SARS-CoV-2 PLpro in the interactome network, whereas Level 2 human proteins are indirectly connected to PLpro through the Level 1 proteins (Figure 8).

Twenty-seven host proteins directly interact with PLpro (Level 1). The functions of these host proteins include transcription, ribosomal function, actin-cytoskeleton, mitochondrial function-ADP ribosylation, cell cycle, RNA processing, endoplasmic reticulum and function, phospholipid and fatty acid synthesis, ubiquitination, histone function, chromatin remodeling and nucleosome function, zinc binding (TRIM13), and antiviral immunity. All these processes are highly relevant to the interaction between the SARS-CoV-2 virus and the human host. Among these Level 1 proteins, 4 are hub-bottleneck proteins (RPL30, NOB1, NDUFS1, RPL21), and 23 are bottleneck proteins (SRPR, FDFT1, ACSL3, EMC8, NDC1, STIM1, STIM2, ARPC1B, HIST1H1B, AGPAT2, STT3A, DDRGK1, EMC1, TRIM13, CCNB2, ARL6IP5, LSM1, ESPL1, SLC27A4, AAAS, EMC7,

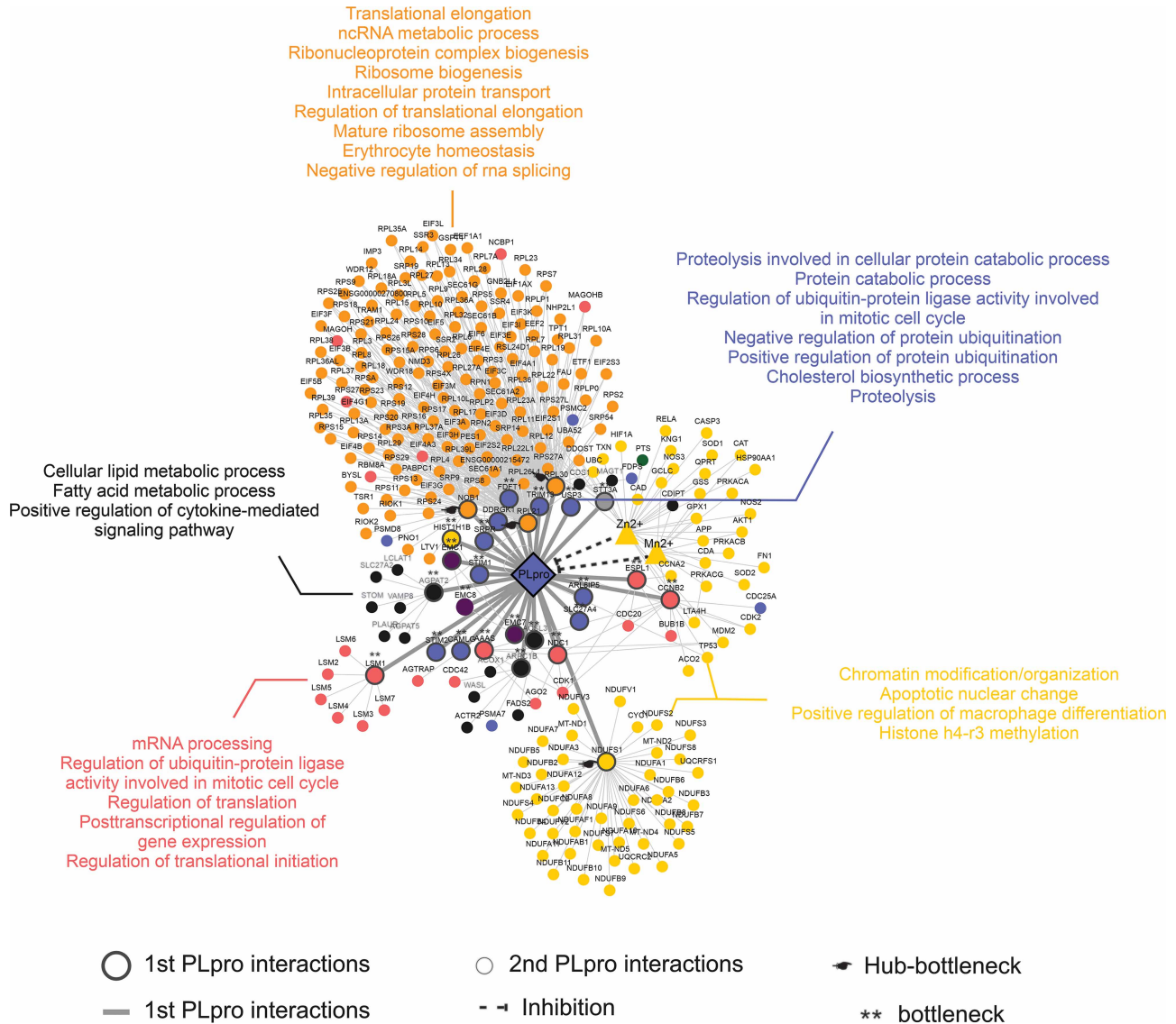


**Figure 8. Protein clusters highlighting interactions between PLpro and host core proteins with level 1 and level 2 interactions.**

The large circles correspond to the central proteins (Hub-bottleneck — black hand pointing, bottleneck — double asterisks). The first interactions of PLpro are highlighted with wide grey connectors. The smaller circles correspond to second-degree interactions with PLpro (second PLpro neighborhood). The yellow triangles represent  $Zn^{2+}$  and  $Mn^{2+}$ . The dashed black lines represent the inhibitory activity of  $Zn^{2+}$  and  $Mn^{2+}$  on PLpro. The collective functional annotation of each protein cluster in the interactome for both level 1 and level 2 interactions between PLpro and host proteins is noted. The figure was constructed by integrating centrality, cluster, and functional enrichment analyses using the Cytoscape program [35]. Edits were performed in CoreIDRAW®.

CAMLG, USP3). Bottleneck proteins function as connections between functional clusters and have high betweenness centrality; i.e. many short paths in the network pass through these points. Thus, bottleneck proteins provide key connections in the network and are more likely to be essential proteins than hub proteins [36]. Hub-bottleneck proteins are hub proteins that are directly connected to bottleneck proteins; they are frequently central proteins that link multiple complexes or peripheral components of central complexes [36].

Previous studies have identified RPL8, RPSA, RPL12, EEF1A1, RPL6, RPL15, RPS11, RPS16, RPL11, and RPS15A [37–42] as the top 10 Level 1 hub proteins interacting with SARS-CoV-2 PLpro [43]; KEGG pathway analysis by Ghosh et al. [43] showed that these proteins are involved in ribosome function and RNA transport. Based on the high degree of interaction of the hub proteins in the present analysis, we can add three hub-

bottleneck proteins — RPL30, NOB1 and RPL21 — to the proteins reported by Ghosh et al. The networks of these three hub bottleneck proteins appear to be involved in translational elongation and its regulation, ribonucleoprotein complex biogenesis, intracellular protein transport RNA splicing and ribosome assembly (Figure 8). In addition, we identified a major cluster connected to NDUFS1, which is directly connected to PLpro (Figure 8). NDUFS1 is a multi-subunit NADH:ubiquinone oxidoreductase (complex I; EC 1.6.5.3) and is the first enzyme complex in the mitochondrial electron transport chain. All of the proteins in NDUFS1's network appear to be involved in the mitochondrial electron transport chain, chromatin reorganization, regulation of macrophage differentiation and histone h4-r3 methylation, which are highly relevant to SARS-CoV-2 infection.

We also analyzed the interactions of manganese and zinc with host proteins that interact with SARS-CoV-2 PLpro. Both clearly interact with host metalloproteinases, proteins that are functionally relevant to antiviral and innate immunity processes, in addition to host proteins involved in the regulation of the influx and efflux of metal ions from cells (e.g. CASP3, SOD-1, HSP90AA1, and NOS-3). Metal ion regulation, which is integral to immunity against viral infection, is subverted by SARS-CoV-2 infection. Of particular note is the STRING network of the bottleneck protein CCNB2 [44,45], which comprises 10 proteins, including CCNA2, CDK2, CDC25A and BUB1B. These four proteins are mainly involved in cell cycle function and control of G1/S and G2/M transition phases of the cell cycle. They also show a close interaction with  $Mn^{2+}$  (Figure 8). Manganese is an essential nutrient for bacteria and viruses and an essential cofactor for numerous cellular processes. When viruses infect a vertebrate host, a hostile environment with minimal bioavailable manganese is created via sequestration of manganese at the focus of infection. To combat this host strategy, pathogens can express high-affinity manganese importers that are vital in inducing virulence [46]. The host–pathogen interface is largely a battle for manganese, which shapes the pathogenesis of infection. Thus, the network of CCNB2 is highly relevant during the infectious process induced by SARS-CoV-2, and its interaction with PLpro and manganese is not coincidence but is functionally relevant to SARS-CoV-2 infection.

## Discussion

Several targets have been identified for the development of antivirals against SARS-CoV-2. The most promising are the viral proteases. Both PLpro and the main protease (Mpro) are vital in the processing of the viral polyproteins (pp1a and pp1ab), which is a prerequisite for the maturation of the non-structural viral proteins [47,48]. PLpro, which originates from the membrane anchored multi-domain protein nsp3 [15], also suppresses antiviral innate immunity by reversing ubiquitination and ISGylation [9,24,49–52]. This dual functionality of PLpro makes it an attractive antiviral drug target [19,53,54]. Moreover, PLpro is highly conserved among coronaviruses, with 82% and 30% amino acid sequence identity of SARS-CoV-2 PLpro with SARS-CoV PLpro and MERS PLpro, respectively, suggesting that drugs targeting PLpro could be used to prevent and treat a broad range of coronavirus infections.

Multiple cysteine residues are essential for the function and stability of PLpro. In addition to the catalytic Cys111 residue, Cys189, Cys192, Cys223 and Cys226 in the finger domain of PLpro tetrahedrally coordinate a zinc cation that is essential for structural stability and protease activity [9,24]. Consistent with this structural role of zinc, zinc-ejector drugs reduce PLpro activity. However, zinc has also been shown to inhibit SARS-CoV-1 and MERS PLpro [28,34]. Zinc has been utilized clinically to reduce the symptoms of COVID-19 and enhance antiviral immunity against SARS-CoV-2, and patients with severe COVID-19 symptoms have been shown to possess low zinc levels [55–57]. Moreover, zinc possesses antiviral properties against various coronaviruses, hepatitis C virus, and HIV [56,58,59]. Beyond PLpro, zinc inhibits both SARS-CoV-1 and equine arterivirus RNA polymerase [60], and an  $IC_{50}$  of zinc of 50  $\mu M$  has been reported for SARS-CoV-1 RNA-dependent RNA polymerase. Overall, these findings suggest that zinc in the right form and quantity can inhibit different biological targets essential for viral replication, including RNA synthesis, topoisomerase, and polyprotein processing [59].

The effects of zinc and other metal ions on SARS-CoV-2 PLpro have not been comprehensively investigated. To address this gap, this study investigated the effects of various divalent metal cations on the activity and biophysical properties of PLpro, as a mechanistic and structural understanding of the effects of metal ions is necessary to develop effective antiviral drug combinations.

## Zinc and manganese inhibit PLpro activity

In addition to zinc, the effects of manganese, magnesium, iron, and calcium, which are commonly found in the body and bind to proteins in coordination complexes, were investigated [61]. Neither magnesium nor iron impacted PLpro activity, and the inhibitory effect of calcium was too weak to warrant further investigation. The

IC<sub>50</sub> of zinc was ~0.4 mM when 0.5 mM EDTA was included in the assay. This value is much higher than the IC<sub>50</sub> of 1.3 μM reported for SARS-CoV PLpro [28,34]. However, this discrepancy may reflect the absence of EDTA in the assays of SARS-CoV PLpro. In the presence of increasing concentrations of EDTA, the IC<sub>50</sub> of zinc increased, indicating that zinc inhibits PLpro only after saturating the zinc-EDTA interaction. The extrapolation of the linear fit of the IC<sub>50</sub> of zinc as a function of EDTA concentration yielded an estimated IC<sub>50</sub> of zinc of 14 μM in the absence of EDTA (Figure 5c). This analysis indicates a strong inhibitory effect of zinc on SARS-CoV-2 PLpro.

Our study is the first to report an inhibitory effect of manganese on SARS-CoV-2 PLpro; a previous screen of divalent metal ions found that SARS-CoV PLpro was not inhibited by manganese [28]. The use of manganese along with other metal ions and vitamins to relieve the symptoms of COVID-19 has been proposed [62]. The IC<sub>50</sub> of manganese for PLpro was 2.6 mM, higher than that for zinc. In addition, manganese exhibited a mixed inhibition pattern, indicating that manganese metal ions bind to either free enzyme or the enzyme-substrate complex at a site other than the active site. Unfortunately, a similar analysis of the inhibition pattern of zinc was experimentally unfeasible due to the steep slopes of the IC<sub>50</sub> curves for zinc and its narrow inhibition range.

In this study, adding EDTA was essential for PLpro activity, and a concentration of 0.5 mM EDTA was found to be optimal, consistent with previous work [33]. The requirement for EDTA can be explained by the observed inhibition of PLpro by zinc and manganese; slight traces of zinc (or other metals) in the purified enzyme or buffer are sufficient to inhibit SARS-CoV-2 PLpro. Upon increasing the zinc concentration beyond the EDTA concentration, PLpro activity dropped sharply. As a result, the acquired IC<sub>50</sub> values were lower than the concentration of EDTA. The true IC<sub>50</sub>s of ZnSO<sub>4</sub> and ZnCl<sub>2</sub> are lower than the apparent IC<sub>50</sub>s determined in the presence of 0.5 mM EDTA reported here of 0.35 ± 0.01 mM and 0.42 ± 0.02 mM, respectively; we estimated an IC<sub>50</sub> for ZnCl<sub>2</sub> of 14 μM in the absence of EDTA.

The binding affinity of PLpro for zinc and manganese was assessed by measuring intrinsic tryptophan fluorescence as a function of metal ion concentration. Consistent with the effects of zinc and manganese on activity, the K<sub>D</sub> values for ZnSO<sub>4</sub> (K<sub>D</sub>, 0.48 ± 0.21 mM) and ZnCl<sub>2</sub> (K<sub>D</sub>, 0.27 ± 0.17 mM) were 10-fold lower than that for MnCl<sub>2</sub> (K<sub>D</sub>, 2.74 ± 0.60 mM), indicating higher binding affinity of PLpro for zinc compared with manganese. Increasing the concentration of zinc or manganese quenched intrinsic tryptophan fluorescence without shifting λ<sub>max</sub>, implying that the electronic environment around the tryptophan residues of PLpro did not change enough to shift the emission signal of tryptophan [63–65]. Since the zinc finger domain is integral to the structural stability of PLpro, we assume that no zinc replacement occurred in this domain in the intrinsic fluorescence experiments.

## Metal binding induces conformational changes and reduces the thermodynamic stability of PLpro

Due to the large number of cysteine residues and the chemical nature of the surface of PLpro, this protease is capable of binding a variety of ions, including non-structural zinc ions [60]. In the present study, far-UV CD spectroscopy confirmed that the addition of zinc or manganese induced conformational changes in SARS-CoV-2 PLpro while preserving a significant amount of secondary structure (Figure 7b,c). A large structural shift in the zinc-binding domain is also evident when the crystal structure of SARS-CoV-2 PLpro is compared with that of MERS PLpro [59,60]. The conformational changes observed by CD spectroscopy upon the addition of zinc or manganese reflect the formation of a new inhibited state of SARS-CoV-2 PLpro, which may explain the molecular mechanism of PLpro inhibition by zinc and manganese.

Overall, adding zinc or manganese decreased the thermodynamic stability of PLpro and its melting point as assessed by DSC. However, a pronounced change in stability was observed only upon increasing the concentration of metal ions to 0.5 mM. The substantial decrease in Δ*H*<sub>cal</sub> of PLpro with increasing ZnSO<sub>4</sub> concentration but no change in *T*<sub>m</sub> indicates that zinc alters the protein bonding characteristics of PLpro. Proteins with hydrophobic character exhibit negative exothermic peaks on DSC thermograms, whereas polar proteins yield positive endothermic peaks [66,67]. The decrease in the Δ*H*<sub>cal</sub> of PLpro implies changes in protein bonding behavior from hydrogen-bonding and polar to hydrophobic interactions, indicating that high zinc concentrations alter the structural characteristics of SARS-CoV-2 PLpro.

## Intrinsic relationship between metal ions and host–virus interactions

Studying the centrality of proteins in interaction networks is crucial to identify essential elements of the biosystem. Perturbations (deletion, overexpression, etc.) of these elements can have a large impact on the biosystem.

Proteins with high network connectivity, i.e. hubs, are considered more important for the system than those with low connectivity. There are many proteins in the  $Zn^{2+}$  and  $Mn^{2+}$  networks, and in this study, we only selected hub proteins encompassing PLpro,  $Zn^{2+}$  and  $Mn^{2+}$  for analysis and discussion. For instance, both  $Zn^{2+}$  and  $Mn^{2+}$  interact with HSP90AA1 (heat shock protein 90 kDa alpha, class A, member 1), also known as HSP90alpha, a member of the large family of HSP molecular chaperones (Figure 8). HSPs are involved in responses to diverse sources of stress that disrupt protein conformation, such as ethanol, arsenite, cadmium, zinc, copper, mercury, sulfhydryl reagents, calcium ionophores, steroid hormones, chelating agents, and viruses [68].

$Zn^{2+}$  directly influences apoptotic regulators, especially the caspase family of enzymes, which also indirectly control the decline in intracellular  $Zn^{2+}$  below a critical threshold. Low intracellular  $Zn^{2+}$  levels may not only trigger pathways leading to caspase activation but may also facilitate the process by which caspases are activated by viruses — an epigenetic process that viruses use to exploit the host antiviral immunity. Studies of airway epithelial cells have shown that  $Zn^{2+}$  colocalizes with the precursor form of caspase-3, mitochondria and microtubules, suggesting that  $Zn^{2+}$  is critically positioned to control apoptosis. In the interactome,  $Zn^{2+}$  is connected to caspase-3, a protein subverted by SARS-CoV-2 PLpro [69]. Another member of the  $Zn^{2+}$  and PLpro network is superoxide dismutase (SOD1). SOD1 is abundant in cells throughout the body and binds copper and zinc to break down toxic charged oxygen molecules called superoxide radicals. Plasma proteomics analyses have revealed that SOD1 is a possible predictor of COVID-19 progression [70].

The  $Zn^{2+}$  and PLpro network also includes nitric oxide synthase (NOS-3), which produces nitric oxide (NO). NO plays important roles in the neuronal, muscular, cardiovascular, and immune systems and in viral infections. Zinc is an important structural element of NOS and inhibits its catalytic activity. Zinc down-regulates the mRNA and protein expression of inducible nitric oxide synthase (iNOS) and decreases cytokine-mediated activation of the iNOS promoter. Zinc-mediated regulation of iNOS expression in endothelial cells is mainly attributed to the inhibition of NF- $\kappa$ B transactivation activity. Decreases in iNOS activity are observed during SARS-CoV-2 infection, and COX-2 expression seems to diminish NF- $\kappa$ B and AP-1 activation [71,72]. Decreased bioavailability of NO and increased inflammation are hallmarks of endothelial dysfunction and are prominent in SARS-CoV-2 infection (especially during acute respiratory distress syndrome (ARDS)), which is thought to be an endothelial disease. During severe SARS-CoV-2 infection and ARDS, a cytokine storm accompanied by decreases in NO, IL-6, MCP-1, TNF-alpha, IL-1B and IFN-gamma production in macrophages is observed [72]. Clinical studies of SARS-CoV-2 infection have shown that NO inhibits virus entry into host cells, viral replication, the host immune response, and subsequent thromboembolic complications. Therefore, restoring NO bioavailability may hold potential as a preventive or early treatment option for COVID-19 [73].

The interactome is consistent with the fact that zinc acts at multiple levels in cells to combat SARS-CoV-2, which makes it difficult to define a single cellular or biochemical mechanism of action. Recent studies have shown that different zinc salts possess antiviral activity against SARS-CoV-2 [74,75]. The antiviral activity of zinc reflects a series of effects on viral binding, penetration, uncoating, and replication [76]. As a membrane stabilizer, zinc directly inhibits coronaviral entry, polyprotein processing, and RNA-dependent RNA polymerase (RdRP) activity [77], consistent with our interactome analysis. Moreover, zinc is involved in the production of interleukin-12 (IL-12) and interferon (IFN) by stimulating macrophages. In particular, IL-12 activates natural killer and cytotoxic T cells to effectively combat the virus. The interactome data linking  $Zn^{2+}$  and  $Mn^{2+}$  with the positive regulation of macrophage differentiation strongly align with these effects.

Finally,  $Mn^{2+}$  not only inhibits PLpro but also directly interacts with CCNB2, which is associated with the regulation of ubiquitin-protein ligase activity involved in the mitotic cell cycle and is highly relevant in epigenetic modulation and host antiviral activity in response to SARS-CoV-2. The importance of CCNB2 and its functional network [44,45], which includes 10 proteins, is further supported by the fact that four of those proteins — CCNA2, CDK2, CDC25A and BUB1B — have close interactions with  $Mn^{2+}$  in the interactome (Figure 8). Interestingly, all 4 proteins control the G1/S and G2/M transition phases of the cell cycle and depend strongly on manganese availability [46]. Their interaction with PLpro further emphasizes that SARS-CoV-2 subverts host cell cycle regulation through a battle for manganese — an essential nutrient for a number of cellular processes and host immunity. This finally cements the biological basis of metal ions (mainly  $Zn^{2+}$  and  $Mn^{2+}$ ) and their intrinsic role in viral infections, along with their therapeutic use in drug formulations in conjunction with antiviral agents.

## Conclusion

Zinc is widely used to control viral infections. The present study demonstrates that  $Zn^{2+}$  and  $Mn^{2+}$  suppress PLpro activity and thus may provide synergistic support in treating COVID-19 if used as supplements along with antiviral drugs. As the study here has shown strong evidence in favor of the biochemical activity of metal ions, we believe that future therapeutic strategies would benefit from combining  $Zn^{2+}$  and  $Mn^{2+}$  with antiviral drugs in effectively controlling SARS-CoV-2 infection.

## Materials and methods

### Expression and purification of PLpro

The recombinant PLpro gene with an N-terminal His<sub>6</sub> tag was introduced into the pET-28b (+) bacterial expression vector by GenScript, Inc. (Piscataway, NJ). The vector was used to transform *E. coli* BL21-CodonPlus-RIL (Stratagene) for protein expression. The inoculated culture (3–6 L) was grown at 30 °C in lysogeny broth (LB) with 100 mg/L kanamycin, 50 mg/L chloramphenicol, and 1  $\mu$ M  $ZnCl_2$  until the absorbance at 600 nm reached 0.5. The temperature was then reduced to 15°C, and protein expression was induced overnight (14–16 h) by adding 1 mM IPTG. The cells were pelleted by centrifugation at 12 000×g and 4°C for 10 min in an Avanti J26-XPI centrifuge (Beckman Coulter Inc.). The cell pellets were homogenized in lysis buffer (25 mM Tris, 150 mM NaCl, 5 mM imidazole, 3 mM  $\beta$ -mercaptoethanol ( $\beta$ ME), and 0.1% protein inhibitor cocktail (Sigma–Aldrich: P8849) before sonication on ice. The cell lysate was then centrifuged at 40 000×g and 4°C for 45 min. The supernatant was loaded onto a nickel column pre-equilibrated with binding buffer (25 mM Tris, 150 mM NaCl, 5 mM imidazole, and 3 mM  $\beta$ ME). The column was washed with binding buffer supplemented with 25 mM imidazole, followed by elution with binding buffer supplemented with 300 mM imidazole. The nickel column fractions containing PLpro were pooled and loaded onto a HiLoad Superdex 200 size-exclusion column (GE Healthcare) on an ÄKTA pure 25 chromatography system (Cytiva, U.S.A.). The gel filtration column was pre-equilibrated with 20 mM HEPES pH 7.5, 150 mM NaCl, and 0.5 mM tris(2-carboxyethyl)phosphine (TCEP). The PLpro-containing fractions were collected and concentrated to ~150  $\mu$ M. The sample concentration and purity were determined by the Bradford assay and SDS-PAGE, respectively.

### Enzymatic assay and inhibition studies

PLpro enzymatic activity and inhibition analyses were performed using a Cytation 5 multi-mode microplate reader (BIOTEK Instruments, Winooski, VT). The peptide substrate contained the PLpro cleavage site Leu-Arg-Gly-Gly flanked by a fluorescent AMC (7-amino-4-methyl coumarin) tag and corresponding quencher CBZ (carbobenzoxy) (i.e. Z-LRGG-AMC). The proteolytic reaction was initiated by adding 0.5  $\mu$ M PLpro enzyme to the peptide in buffer (50 mM HEPES pH 7.5, 0.5 mM EDTA, and 0.5 mM TCEP) containing 2% DMSO to enhance the solubility of the peptide [78]. The PLpro reaction was monitored in a 96-well microplate at 25 °C for 10 min at excitation and emission wavelengths of 340 nm and 487 nm, respectively. Cleavage of the peptide substrate by PLpro resulted in an increase in the AMC fluorescent signal.

The inhibitory effects of zinc, manganese, and calcium on the proteolytic activity of PLpro were investigated by determining their half maximal inhibitory concentrations ( $IC_{50}$ s). The  $IC_{50}$ s of the different metal ions were determined at a fixed peptide substrate concentration of 135  $\mu$ M by serially diluting the metal by a factor of 1.25 from 0  $\mu$ M to 600  $\mu$ M for  $ZnCl_2$  and  $ZnSO_4$  and from 0 mM to 10 mM for  $CaCl_2$  and  $MnCl_2$ . The  $IC_{50}$  data were fit to a four-parameter dose-response (variable slope) model in GraphPad Prism 9 (GraphPad, San Diego, CA).

For the inhibition studies, the peptide substrate concentration was varied at 45  $\mu$ M, 55  $\mu$ M, 75  $\mu$ M, 110  $\mu$ M, 250  $\mu$ M, and 800  $\mu$ M at different fixed metal ion concentrations around their  $IC_{50}$  values ranging from 300  $\mu$ M to 480  $\mu$ M for zinc salts and 2 mM to 10 mM for  $MnCl_2$ . The inhibition data for  $MnCl_2$  were fit to a mixed-inhibition Michaelis–Menten equation using SigmaPlot (Systat Software, Inc., San Jose, CA):

$$v = \frac{V_{max}}{\left(\frac{K_m}{[S]}\right) \left(1 + \frac{[I]}{K_i}\right) + \left(1 + \frac{[I]}{K_i}\right)}$$

where  $v$  and  $V_{max}$  are the measured initial rate and maximum rate, respectively,  $[S]$  and  $[I]$  are the substrate

and inhibitor concentrations, respectively,  $K_m$  is the Michaelis constant for the substrate, and  $K_i$  is the inhibition constant.

### Tryptophan fluorescence spectroscopy (TFS) scans of PLpro

TFS measurements of PLpro were performed in a quartz cuvette in a fluorescence spectrometer (HORIBA Fluorometer4, HORIBA Instruments Incorporated, Edison, NJ) with excitation and emission pathlengths of 4 mm and 10 mm, respectively. The emission spectra were acquired from 300 nm to 450 nm with slit width of 1 nm at an excitation wavelength of 290 nm. The temperature was maintained at 25°C, and the PLpro protease concentration was 10  $\mu\text{M}$  in 50 mM HEPES pH 7.5, and 0.5 mM TCEP. TFS scans were collected upon titrating different concentrations of  $\text{ZnCl}_2$  and  $\text{ZnSO}_4$  in two ranges: from 0  $\mu\text{M}$  to 2  $\mu\text{M}$  and from 2  $\mu\text{M}$  to 1000  $\mu\text{M}$ . The  $\text{MnCl}_2$  concentration was varied from 5  $\mu\text{M}$  to 5000  $\mu\text{M}$ . The change in the tryptophan fluorescence signal was plotted as a function of metal ion concentration to determine the binding affinity constant ( $K_D$ ) of metal ions to PLpro. The plots were fit to a one-site binding model using GraphPad Prism 9. In parallel with the ion titration scans, TFS scans were obtained by adding buffer only to account for the effect of protein dilution upon addition of the metal ion. All measurements were performed in triplicate.

### Differential scanning calorimetry (DSC)

The thermodynamic stability of PLpro was assessed by DSC in the presence or absence of metal ions as well as EDTA using a Nano DSC instrument (TA Instruments) at 0.25 mM and 0.5 mM  $\text{ZnSO}_4$ ,  $\text{ZnCl}_2$ , and  $\text{MnCl}_2$ . The instrument was calibrated using chicken egg white lysozyme, a known external Nano DSC standard that is part of the TA Instruments test kit (602198.901). The DSC scans were acquired at a PLpro concentration of 30  $\mu\text{M}$  in buffer containing 50 mM HEPES pH 7.5 and 0.5 mM TCEP in the presence and absence of 0.5 mM EDTA. The protein samples were heated from 15°C to 75°C at a scan rate of 1°C/min and 3 atm pressure. The DSC thermogram was corrected by subtracting the baseline and converted to a plot of excess heat capacity ( $C_p$ ) as a function of temperature. A corresponding buffer baseline was collected for each measurement by applying a second heating scan on the protein sample. The melting temperature ( $T_m$ ) was determined at the maximum temperature of the thermal transition, and the calorimetric enthalpy ( $\Delta H_{\text{cal}}$ ) of the transition was estimated from the area under the thermal transition using Nano Analyzer software (TA Instruments). DSC measurements were performed in duplicate.

### Far-UV circular dichroism (CD) spectroscopy

CD spectra of PLpro were collected in 10 mM Tris pH 7.5. Phosphate buffer was not used because precipitation of the enzyme was observed when PLpro was incubated with phosphate buffer. Since zinc phosphate is water insoluble, the low stability of PLpro in phosphate buffer may be due to instability of the structural zinc in the zinc-binding domain, which has been shown to be important for the structural stability and protease activity of PLpro [9,24]. Scans were collected in a Chirascan CD spectrometer (Applied Photophysics) calibrated with aqueous camphor-10-sulfonic acid (CSA) from 200 nm to 260 nm at a scanning speed of 10 nm/sec and bandwidth of 1 nm using 30  $\mu\text{M}$  PLpro in a 1 mm quartz cuvette. The temperature was maintained at 25°C and 80°C to acquire spectra of the native and denatured states of PLpro, respectively. All CD scans were corrected for buffer and substrate background, and five CD scans were averaged to obtain each spectrum.

### Interactome analysis

Interactions between SARS-CoV-2 and *Homo sapiens* proteins were taken from the BIOGRID database. Since the STRING database has a more standardized scoring system [44], we used this database to identify high-confidence interactions (>900) between NSP3/PLpro and human proteins. This interactome (unpublished data) has been used previously by our group in studies of SARS-CoV-2 replication proteins.

The central proteins for the biosystem (hub, bottleneck, and hub-bottleneck) were determined based on betweenness and degree centrality using the betweenness and degree functions of the igraph package [79]. Hubs are proteins with high degree centrality, bottlenecks are proteins with high betweenness, and hub-bottlenecks are hub proteins that are directly connected to a bottleneck protein. Cluster analysis was also performed in the R environment using the fastgreedy community function [79,80]. The focus was on the cluster of PLpro-related proteins. In this cluster, only the first and second levels of interactions of PLpro with central proteins were highlighted. For this group of proteins, functional enrichment analysis was performed to identify biological processes related to central proteins interacting with PLpro. For this purpose, the plugin BINGO

from the Cytoscape program was used with the hypergeometric test applying the Benjamini & Hochberg false discovery rate (FDR) correction test for multiple comparisons [35,81].

### Data Availability

The authors declare that all data that support the findings of this study are available within the paper files.

### Competing Interests

The authors declare that there are no competing interests associated with the manuscript.

### Funding

This work was supported by New York University Abu Dhabi through research funds to the lab of Prof. Rabeh in addition to the COVID-19 Facilitator Research Fund (grant number: ADC05).

### CRedit Author Contribution

**Wael M. Rabeh:** Conceptualization, Formal analysis, Supervision, Funding acquisition, Methodology, Writing — original draft, Project administration, Writing — review and editing. **Cameron Lee Shetler:** Data curation, Formal analysis, Validation, Writing — original draft. **Juliana C. Ferreira:** Data curation. **Thyago H. S. Cardoso:** Data curation, Software. **Edson M.A. Silva:** Software, Formal analysis. **Nitin K. Saksena:** Data curation, Writing — original draft.

### Acknowledgements

This research was partially carried out using the Core Technology Platforms resources at New York University Abu Dhabi.

### Abbreviations

3CLpro, 3-chymotrypsin-like cysteine protease;  $K_D$ , binding affinity constant;  $\Delta H_{cal}$ , calorimetric enthalpy; CD, circular dichroism; COVID-19, coronavirus disease 2019; DSC, differential scanning calorimetry;  $\lambda_{em}$ , emission wavelength;  $\lambda_{ex}$ , excitation wavelength;  $IC_{50}$ , half maximal inhibitory concentration;  $K_i$ , inhibition constant;  $\lambda_{max}$ , maximum tryptophan emission wavelength;  $T_m$ , melting temperature; MERS-CoV, Middle East respiratory syndrome coronavirus; nsps, non-structural proteins; PLpro, papain-like protease; ORFs, open reading frames; SARS-CoV, severe acute respiratory syndrome coronavirus; SARS-CoV-2, severe acute respiratory syndrome coronavirus 2; TFS, tryptophan fluorescence spectroscopy.

### References

- 1 WHO. (2022) *World Health Organization Coronavirus (COVID-19) Dashboard*, World Health Organization, Geneva, Switzerland
- 2 Zhou, P., Yang, X.L., Wang, X.G., Hu, B., Zhang, L., Zhang, W. et al. (2020) A pneumonia outbreak associated with a new coronavirus of probable bat origin. *Nature* **579**, 270–273 <https://doi.org/10.1038/s41586-020-2012-7>
- 3 Zhu, N., Zhang, D., Wang, W., Li, X., Yang, B., Song, J. et al. (2020) A novel coronavirus from patients with pneumonia in China, 2019. *N. Engl. J. Med.* **382**, 727–733 <https://doi.org/10.1056/NEJMoa2001017>
- 4 Astuti, I. and Ysrafil, (2020) Severe acute respiratory syndrome coronavirus 2 (SARS-CoV-2): an overview of viral structure and host response. *Diabetes Metab. Syndr.* **14**, 407–412 <https://doi.org/10.1016/j.dsx.2020.04.020>
- 5 Malik, A. and Alsenaidy, M.A. (2017) MERS-CoV papain-like protease (PLpro): expression, purification, and spectroscopic/thermodynamic characterization. *3 Biotech.* **7**, 100 <https://doi.org/10.1007/s13205-017-0744-3>
- 6 V'kovski, P., Kratzel, A., Steiner, S., Stalder, H. and Thiel, V. (2021) Coronavirus biology and replication: implications for SARS-CoV-2. *Nat. Rev. Microbiol.* **19**, 155–170 <https://doi.org/10.1038/s41579-020-00468-6>
- 7 Hu, B., Guo, H., Zhou, P. and Shi, Z.L. (2020) Characteristics of SARS-CoV-2 and COVID-19. *Nat. Rev. Microbiol.* **19**, 141–154 <https://doi.org/10.1038/s41579-020-00459-7>
- 8 Kim, D., Lee, J.-Y., Yang, J.-S., Kim, J.W., Kim, V.N. and Chang, H. (2020) The architecture of SARS-CoV-2 transcriptome. *Cell* **181**, 914–921. <https://doi.org/10.1016/j.cell.2020.04.011>
- 9 Klemm, T., Ebert, G., Calleja, D.J., Allison, C.C., Richardson, L.W., Bernardini, J.P. et al. (2020) Mechanism and inhibition of the papain-like protease, PLpro, of SARS-CoV-2. *EMBO J.* **39**, e106275 <https://doi.org/10.15252/embj.2020106275>
- 10 Moustaqil, M., Ollivier, E., Chiu, H.P., Van Tol, S., Rudolphi-Soto, P., Stevens, C. et al. (2021) SARS-CoV-2 proteases PLpro and 3CLpro cleave IRF3 and critical modulators of inflammatory pathways (NLRP12 and TAB1): implications for disease presentation across species. *Emerg. Microbes Infect.* **10**, 178–195 <https://doi.org/10.1080/22221751.2020.1870414>
- 11 Chen, X., Yang, X., Zheng, Y., Yang, Y., Xing, Y. and Chen, Z. (2014) SARS coronavirus papain-like protease inhibits the type I interferon signaling pathway through interaction with the STING-TRAF3-TBK1 complex. *Protein Cell* **5**, 369–381 <https://doi.org/10.1007/s13238-014-0026-3>
- 12 Devaraj, S.G., Wang, N., Chen, Z., Chen, Z., Tseng, M., Barretto, N. et al. (2007) Regulation of IRF-3-dependent innate immunity by the papain-like protease domain of the severe acute respiratory syndrome coronavirus. *J. Biol. Chem.* **282**, 32208–32221 <https://doi.org/10.1074/jbc.M704870200>



- 13 Yang, X., Chen, X., Bian, G., Tu, J., Xing, Y., Wang, Y. et al. (2014) Proteolytic processing, deubiquitinase and interferon antagonist activities of Middle East respiratory syndrome coronavirus papain-like protease. *J. Gen. Virol.* **95**, 614–626 <https://doi.org/10.1099/vir.0.059014-0>
- 14 Ratia, K., Saikatendu, K.S., Santarsiero, B.D., Barretto, N., Baker, S.C., Stevens, R.C. et al. (2006) Severe acute respiratory syndrome coronavirus papain-like protease: structure of a viral deubiquitinating enzyme. *Proc. Natl Acad. Sci. U.S.A.* **103**, 5717–5722 <https://doi.org/10.1073/pnas.0510851103>
- 15 Ratia, K., Pegan, S., Takayama, J., Sleeman, K., Coughlin, M., Baliji, S. et al. (2008) A noncovalent class of papain-like protease/deubiquitinase inhibitors blocks SARS virus replication. *Proc. Natl Acad. Sci. U.S.A.* **105**, 16119–16124 <https://doi.org/10.1073/pnas.0805240105>
- 16 Li, G. and De Clercq, E. (2020) Therapeutic options for the 2019 novel coronavirus (2019-nCoV). *Nat. Rev. Drug Discov.* **19**, 149–150 <https://doi.org/10.1038/d41573-020-00016-0>
- 17 Park, B.K., Kim, J., Park, S., Kim, D., Kim, M., Baek, K. et al. (2021) MERS-CoV and SARS-CoV-2 replication can be inhibited by targeting the interaction between the viral spike protein and the nucleocapsid protein. *Theranostics* **11**, 3853–3867 <https://doi.org/10.7150/thno.55647>
- 18 Shin, D., Mukherjee, R., Grewe, D., Bojkova, D., Baek, K., Bhattacharya, A. et al. (2020) Papain-like protease regulates SARS-CoV-2 viral spread and innate immunity. *Nature* **587**, 657–662 <https://doi.org/10.1038/s41586-020-2601-5>
- 19 Baez-Santos, Y.M., St John, S.E. and Mesecar, A.D. (2015) The SARS-coronavirus papain-like protease: structure, function and inhibition by designed antiviral compounds. *Antivir. Res.* **115**, 21–38 <https://doi.org/10.1016/j.antiviral.2014.12.015>
- 20 Gao, X., Qin, B., Chen, P., Zhu, K., Hou, P., Wojdyla, J.A. et al. (2020) Crystal structure of SARS-CoV-2 papain-like protease. *Acta Pharm. Sin. B* **11**, 237–245 <https://doi.org/10.1016/j.apsb.2020.08.014>
- 21 Sargsyan, K., Lin, C.-C., Chen, T., Grauffel, C., Chen, Y.-P., Yang, W.-Z. et al. (2020) Multi-targeting of functional cysteines in multiple conserved SARS-CoV-2 domains by clinically safe Zn-ejectors. *Chem. Sci.* **11**, 9904–9909 <https://doi.org/10.1039/d0sc02646h>
- 22 Doboszewska, U., Wlaź, P., Nowak, G. and Młyniec, K. (2020) Targeting zinc metalloenzymes in coronavirus disease 2019. *Br. J. Pharmacol.* **177**, 4887–4898 <https://doi.org/10.1111/bph.15199>
- 23 Krishna, S.S., Majumdar, I. and Grishin, N.V. (2003) Structural classification of zinc fingers: survey and summary. *Nucleic Acids Res.* **31**, 532–550 <https://doi.org/10.1093/nar/gkg161>
- 24 Barretto, N., Jukneliene, D., Ratia, K., Chen, Z., Mesecar, A.D. and Baker, S.C. (2005) The papain-like protease of severe acute respiratory syndrome coronavirus has deubiquitinating activity. *J. Virol.* **79**, 15189–15198 <https://doi.org/10.1128/JVI.79.24.15189-15198.2005>
- 25 Bosken, Y.K., Cholko, T., Lou, Y.C., Wu, K.P. and Chang, C.A. (2020) Insights into dynamics of inhibitor and ubiquitin-Like protein binding in SARS-CoV-2 papain-Like protease. *Front. Mol. Biosci.* **7**, 174 <https://doi.org/10.3389/fmolb.2020.00174>
- 26 Ma, C., Hu, Y., Townsend, J.A., Lagarias, P.I., Marty, M.T., Kolocouris, A. et al. (2020) Ebselen, disulfiram, carmofur, PX-12, tideglusib, and shikonin are nonspecific promiscuous SARS-CoV-2 main protease inhibitors. *ACS Pharmacol. Transl. Sci.* **3**, 1265–1277 <https://doi.org/10.1021/acspstsci.0c00130>
- 27 Lin, M.H., Moses, D.C., Hsieh, C.H., Cheng, S.C., Chen, Y.H., Sun, C.Y. et al. (2018) Disulfiram can inhibit MERS and SARS coronavirus papain-like proteases via different modes. *Antiviral Res.* **150**, 155–163 <https://doi.org/10.1016/j.antiviral.2017.12.015>
- 28 Han, Y.-S., Chang, G.-G., Juo, C.-G., Lee, H.-J., Yeh, S.-H., Hsu, J.T.-A. et al. (2005) Papain-like protease 2 (PLP2) from severe acute respiratory syndrome coronavirus (SARS-CoV): expression, purification, characterization, and inhibition. *Biochemistry* **44**, 10349–10359 <https://doi.org/10.1021/bi0504761>
- 29 Wang, L., Hu, W. and Fan, C. (2020) Structural and biochemical characterization of SARS-CoV papain-like protease 2. *Protein Sci.* **29**, 1228–1241 <https://doi.org/10.1002/pro.3857>
- 30 Lindner, H.A., Fotouhi-Ardakani, N., Lytvyn, V., Lachance, P., Sulea, T. and Ménard, R. (2005) The papain-Like protease from the severe acute respiratory syndrome coronavirus is a deubiquitinating enzyme. *J. Virol.* **79**, 15199–15208 <https://doi.org/10.1128/JVI.79.24.15199-15208.2005>
- 31 Rut, W., Lv, Z., Zmudzinski, M., Patchett, S., Nayak, D., Snipas, S.J. et al. (2020) Activity profiling and crystal structures of inhibitor-bound SARS-CoV-2 papain-like protease: a framework for anti-COVID-19 drug design. *Sci. Adv.* **6**, eabd4596 <https://doi.org/10.1126/sciadv.abd4596>
- 32 Chen, Z., Cui, Q., Cooper, L., Zhang, P., Lee, H., Chen, Z. et al. (2021) Ginkgolic acid and anacardic acid are specific covalent inhibitors of SARS-CoV-2 cysteine proteases. *Cell Biosci.* **11**, 45 <https://doi.org/10.1186/s13578-021-00564-x>
- 33 Arya, R., Prashar, V. and Kumar, M. (2022) Evaluating stability and activity of SARS-CoV-2 PLpro for high-throughput screening of inhibitors. *Mol. Biotechnol.* **64**, 1–8 <https://doi.org/10.1007/s12033-021-00383-y>
- 34 Lin, M.-H., Chuang, S.-J., Chen, C.-C., Cheng, S.-C., Cheng, K.-W., Lin, C.-H. et al. (2014) Structural and functional characterization of MERS coronavirus papain-like protease. *J. Biomed. Sci.* **21**, 54 <https://doi.org/10.1186/1423-0127-21-54>
- 35 Shannon, P., Markiel, A., Ozier, O., Baliga, N.S., Wang, J.T., Ramage, D. et al. (2003) Cytoscape: a software environment for integrated models of biomolecular interaction networks. *Genome Res.* **13**, 2498–2504 <https://doi.org/10.1101/gr.1239303>
- 36 Yu, H., Kim, P.M., Sprecher, E., Trifonov, V. and Gerstein, M. (2007) The importance of bottlenecks in protein networks: correlation with gene essentiality and expression dynamics. *PLoS Comput. Biol.* **3**, e99 <https://doi.org/10.1371/journal.pcbi.0030059>
- 37 Hu, L., Wang, X., Huang, Y.A., Hu, P. and You, Z.H. (2021) A survey on computational models for predicting protein-protein interactions. *Brief. Bioinform.* **22**, bbab036 <https://doi.org/10.1093/bib/bbab036>
- 38 Auwul, M.R., Rahman, M.R., Gov, E., Shahjaman, M. and Moni, M.A. (2021) Bioinformatics and machine learning approach identifies potential drug targets and pathways in COVID-19. *Brief. Bioinform.* **22**, bbab120 <https://doi.org/10.1093/bib/bbab120>
- 39 Gupta, P. and Mohanty, D. (2021) SMMPLP: a machine learning-based approach for prediction of modulators of protein-protein interactions and its application for identification of novel inhibitors for RBD:hACE2 interactions in SARS-CoV-2. *Brief. Bioinform.* **22**, bbab111 <https://doi.org/10.1093/bib/bbab111>
- 40 Lian, X., Yang, X., Yang, S. and Zhang, Z. (2021) Current status and future perspectives of computational studies on human-virus protein-protein interactions. *Brief. Bioinform.* **22**, bbab029 <https://doi.org/10.1093/bib/bbab029>
- 41 Ako-Adjei, D., Fu, W., Wallin, C., Katz, K.S., Song, G., Darji, D. et al. (2015) HIV-1, human interaction database: current status and new features. *Nucleic Acids Res.* **43**, D566–D570 <https://doi.org/10.1093/nar/gku1126>
- 42 Kwofie, S.K., Schaefer, U., Sundararajan, V.S., Bajic, V.B. and Christoffels, A. (2011) HCVpro: hepatitis C virus protein interaction database. *Infect. Genet. Evol.* **11**, 1971–1977 <https://doi.org/10.1016/j.meegid.2011.09.001>

- 43 Ghosh, N., Saha, I. and Sharma, N. (2021) Interactome of human and SARS-CoV-2 proteins to identify human hub proteins associated with comorbidities. *Comput. Biol. Med.* **138**, 104889 <https://doi.org/10.1016/j.combiomed.2021.104889>
- 44 Szklarczyk, D., Gable, A.L., Lyon, D., Junge, A., Wyder, S., Huerta-Cepas, J. et al. (2019) STRING v11: protein-protein association networks with increased coverage, supporting functional discovery in genome-wide experimental datasets. *Nucleic Acids Res.* **47**, D607–D613 <https://doi.org/10.1093/nar/gky1131>
- 45 Szklarczyk, D., Gable, A.L., Nastou, K.C., Lyon, D., Kirsch, R., Pyysalo, S. et al. (2021) The STRING database in 2021: customizable protein-protein networks, and functional characterization of user-uploaded gene/measurement sets. *Nucleic Acids Res.* **49**, D605–d612 <https://doi.org/10.1093/nar/gkab835>
- 46 Juttukonda, L. J., and Skaar, E.P. (2017) Manganese and Nutritional Immunity. In *Molecular, Genetic, and Nutritional Aspects of Major and Trace Minerals* (Collins, J., ed.), pp. 377–387, Academic Press, Gainesville, USA
- 47 Lim, K.P., Ng, L.F. and Liu, D.X. (2000) Identification of a novel cleavage activity of the first papain-like proteinase domain encoded by open Reading frame 1a of the coronavirus avian infectious bronchitis virus and characterization of the cleavage products. *J. Virol.* **74**, 1674–1685 <https://doi.org/10.1128/jvi.74.4.1674-1685.2000>
- 48 Hilgenfeld, R. (2014) From SARS to MERS: crystallographic studies on coronaviral proteases enable antiviral drug design. *FEBS J.* **281**, 4085–4096 <https://doi.org/10.1111/febs.12936>
- 49 Békés, M., Rut, W., Kasperkiewicz, P., Mulder, M.P., Ovaa, H., Drag, M. et al. (2015) SARS hcov papain-like protease is a unique Lys48 linkage-specific di-distributive deubiquitinating enzyme. *Biochem. J.* **468**, 215–226 <https://doi.org/10.1042/BJ20141170>
- 50 Békés, M., van der Heden van Noort, G.J., Ekkebus, R., Ovaa, H., Huang, T.T. and Lima, C.D. (2016) Recognition of Lys48-linked di-ubiquitin and deubiquitinating activities of the SARS coronavirus papain-like protease. *Mol. Cell* **62**, 572–585 <https://doi.org/10.1016/j.molcel.2016.04.016>
- 51 Lindner, H.A., Lytvyn, V., Qi, H., Lachance, P., Ziomek, E. and Ménard, R. (2007) Selectivity in ISG15 and ubiquitin recognition by the SARS coronavirus papain-like protease. *Arch. Biochem. Biophys.* **466**, 8–14 <https://doi.org/10.1016/j.abb.2007.07.006>
- 52 Clementz, M.A., Chen, Z., Banach, B.S., Wang, Y., Sun, L., Ratia, K. et al. (2010) Deubiquitinating and interferon antagonism activities of coronavirus papain-like proteases. *J. Virol.* **84**, 4619–4629 <https://doi.org/10.1128/JVI.02406-09>
- 53 Báez-Santos, Y.M., Barraza, S.J., Wilson, M.W., Agius, M.P., Mielech, A.M., Davis, N.M. et al. (2014) X-ray structural and biological evaluation of a series of potent and highly selective inhibitors of human coronavirus papain-like proteases. *J. Med. Chem.* **57**, 2393–2412 <https://doi.org/10.1021/jm401712t>
- 54 Lee, H., Lei, H., Santarsiero, B.D., Gatz, J.L., Cao, S., Rice, A.J., et al. (2015) Inhibitor recognition specificity of MERS-CoV papain-like protease may differ from that of SARS-CoV. *ACS Chem. Biol.* **10**, 1456–1465 <https://doi.org/10.1021/cb500917m>
- 55 Kumar, A., Kubota, Y., Chernov, M. and Kasuya, H. (2020) Potential role of zinc supplementation in prophylaxis and treatment of COVID-19. *Med. Hypotheses* **144**, 109848 <https://doi.org/10.1016/j.mehy.2020.109848>
- 56 Jothimani, D., Kailasam, E., Danielraj, S., Nallathambi, B., Ramachandran, H., Sekar, P. et al. (2020) COVID-19: poor outcomes in patients with zinc deficiency. *Int. J. Infect. Dis.* **100**, 343–349 <https://doi.org/10.1016/j.ijid.2020.09.014>
- 57 Alexander, J., Tinkov, A., Strand, T.A., Alehagen, U., Skalny, A. and Aaseth, J. (2020) Early nutritional interventions with zinc, Selenium and vitamin D for raising anti-viral resistance against progressive COVID-19. *Nutrients* **12**, 2358 <https://doi.org/10.3390/nu12082358>
- 58 Barocas, J.A., So-Armah, K., Cheng, D.M., Lioznov, D., Baum, M., Gallagher, K. et al. (2019) Zinc deficiency and advanced liver fibrosis among HIV and hepatitis C co-infected anti-retroviral naïve persons with alcohol use in Russia. *PLoS ONE* **14**, e0218852 <https://doi.org/10.1371/journal.pone.0218852>
- 59 Skalny, A.V., Rink, L., Ajsuvakova, O.P., Aschner, M., Gritsenko, V.A., Alekseenko, S.I. et al. (2020) Zinc and respiratory tract infections: perspectives for COVID-19 (Review). *Int. J. Mol. Med.* **46**, 17–26 <https://doi.org/10.3892/ijmm.2020.4575>
- 60 te Velthuis, A.J.W., van den Worm, S.H.E., Sims, A.C., Baric, R.S., Snijder, E.J. and van Hemert, M.J. (2010) Zn<sup>2+</sup> inhibits coronavirus and arterivirus RNA polymerase activity in vitro and zinc ionophores block the replication of these viruses in cell culture. *PLoS Pathog.* **6**, e1001176 <https://doi.org/10.1371/journal.ppat.1001176>
- 61 Harding, M.M., Nowicki, M.W. and Walkinshaw, M.D. (2010) Metals in protein structures: a review of their principal features. *Crystallogr. Rev.* **16**, 247–302 <https://doi.org/10.1080/0889311X.2010.485616>
- 62 Hamada, A.M. (2020) Vitamins, omega-3, magnesium, manganese, and thyme can boost our immunity and protect against COVID-19. *Eur. J. Biol. Res.* **10**, 271–295 <https://doi.org/10.5281/zenodo.3990659>
- 63 Vivian, J.T. and Callis, P.R. (2001) Mechanisms of tryptophan fluorescence shifts in proteins. *Biophys. J.* **80**, 2093–2109 [https://doi.org/10.1016/S0006-3495\(01\)76183-8](https://doi.org/10.1016/S0006-3495(01)76183-8)
- 64 Munishkina, L.A. and Fink, A.L. (2007) Fluorescence as a method to reveal structures and membrane-interactions of amyloidogenic proteins. *Biochim. Biophys. Acta* **1768**, 1862–1885 <https://doi.org/10.1016/j.bbame.2007.03.015>
- 65 Sindrewicz, P., Li, X., Yates, E.A., Turnbull, J.E., Lian, L.-Y. and Yu, L.-G. (2019) Intrinsic tryptophan fluorescence spectroscopy reliably determines galectin-ligand interactions. *Sci. Rep.* **9**, 11851 <https://doi.org/10.1038/s41598-019-47658-8>
- 66 Arntfield, S.D. and Murray, E.D. (1981) The influence of processing parameters on food protein functionality I. Differential scanning calorimetry as an indicator of protein denaturation. *Can. Inst. Food Technol. J.* **14**, 289–294 [https://doi.org/10.1016/S0315-5463\(81\)72929-8](https://doi.org/10.1016/S0315-5463(81)72929-8)
- 67 Nawaz, M.H., Ferreira, J.C., Nedyalkova, L., Zhu, H., Carrasco-Lopez, C., Kirmizialtin, S. et al. (2018) The catalytic inactivation of the N-half of human hexokinase 2 and structural and biochemical characterization of its mitochondrial conformation. *Biosci. Rep.* **38**, BSR20171666 <https://doi.org/10.1042/BSR20171666>
- 68 Lindquist, S. (1986) The heat-shock response. *Annu. Rev. Biochem.* **55**, 1151–1191 <https://doi.org/10.1146/annurev.bi.55.070186.005443>
- 69 Truong-Tran, A.Q., Carter, J., Ruffin, R.E. and Zalewski, P.D. (2001) The role of zinc in caspase activation and apoptotic cell death. *Biometals* **14**, 315–330 <https://doi.org/10.1023/a:1012993017026>
- 70 Xu, B., Lei, Y., Ren, X., Yin, F., Wu, W., Sun, Y. et al. (2021) SOD1 is a possible predictor of COVID-19 progression as revealed by plasma proteomics. *ACS Omega* **6**, 16826–16836 <https://doi.org/10.1021/acsomega.1c01375>
- 71 Guimarães, L.M.F., Rossini, C.V.T. and Lameu, C. (2021) Implications of SARS-Cov-2 infection on eNOS and iNOS activity: consequences for the respiratory and vascular systems. *Nitric Oxide* **111–112**, 64–71 <https://doi.org/10.1016/j.niox.2021.04.003>

- 72 Cortese-Krott, M.M., Kulakov, L., Opländer, C., Kolb-Bachofen, V., Kröncke, K.D. and Suschek, C.V. (2014) Zinc regulates iNOS-derived nitric oxide formation in endothelial cells. *Redox Biol.* **2**, 945–954 <https://doi.org/10.1016/j.redox.2014.06.011>
- 73 Kobayashi, J. (2021) Lifestyle-mediated nitric oxide boost to prevent SARS-CoV-2 infection: a perspective. *Nitric Oxide* **115**, 55–61 <https://doi.org/10.1016/j.niox.2021.08.001>
- 74 Tao, X., Zhang, L., Du, L., Lu, K., Zhao, Z., Xie, Y. et al. (2022) Inhibition of SARS-CoV-2 replication by zinc gluconate in combination with hinokitiol. *J. Inorg. Biochem.* **231**, 111777 <https://doi.org/10.1016/j.jinorgbio.2022.111777>
- 75 Kladnik, J., Dolinar, A., Kljun, J., Perea, D., Grau-Expósito, J., Genescà, M. et al. (2022) Zinc pyrithione is a potent inhibitor of PLPro and cathepsin L enzymes with ex vivo inhibition of SARS-CoV-2 entry and replication. *J. Enzyme Inhib. Med. Chem.* **37**, 2158–2168 <https://doi.org/10.1080/14756366.2022.2108417>
- 76 Read, S.A., Obeid, S., Ahlenstiel, C. and Ahlenstiel, G. (2019) The role of zinc in antiviral immunity. *Adv. Nutr.* **10**, 696–710 <https://doi.org/10.1093/advances/nmz013>
- 77 Rani, I., Goyal, A., Bhatnagar, M., Manhas, S., Goel, P., Pal, A. et al. (2021) Potential molecular mechanisms of zinc- and copper-mediated antiviral activity on COVID-19. *Nutr. Res.* **92**, 109–128 <https://doi.org/10.1016/j.nutres.2021.05.008>
- 78 Ferreira, J.C., Fadl, S., Ilter, M., Pekel, H., Rezgüi, R., Sensoy, O. et al. (2021) Dimethyl sulfoxide reduces the stability but enhances catalytic activity of the main SARS-CoV-2 protease 3CLpro. *FASEB J.* **35**, e21774 <https://doi.org/10.1096/fj.202100994>
- 79 Csárdi, G. and Nepusz, T. (2006) The igraph software package for complex network research. *Int. J. Complex Syst.* **1695** <https://igraph.org>
- 80 Clauset, A., Newman, M.E.J. and Moore, C. (2004) Finding community structure in very large networks. *Phys. Rev. E* **70**, 066111 <https://doi.org/10.1103/PhysRevE.70.066111>
- 81 Maere, S., Heymans, K. and Kuiper, M. (2005) BiNGO: a Cytoscape plugin to assess overrepresentation of Gene Ontology categories in Biological Networks. *Bioinformatics* **21**, 3448–3449 <https://doi.org/10.1093/bioinformatics/bti551>